



# PRIMUS+DEEP2: The Dependence of Galaxy Clustering on Stellar Mass and Specific Star Formation Rate at $0.2 < z < 1.2$

Alison L. Coil<sup>1</sup>, Alexander J. Mendez<sup>2</sup>, Daniel J. Eisenstein<sup>3</sup>, and John Moustakas<sup>4</sup>

<sup>1</sup>Center for Astrophysics and Space Sciences, Department of Physics, University of California, 9500 Gilman Drive, La Jolla, CA 92093, USA

<sup>2</sup>Department of Physics and Astronomy, Johns Hopkins University, 3400 North Charles Street, Baltimore, MD 21218, USA

<sup>3</sup>Harvard-Smithsonian Center for Astrophysics, 60 Garden Street, Cambridge, MA 02138, USA

<sup>4</sup>Department of Physics and Astronomy, Siena College, 515 Loudon Road, Loudonville, NY 12211, USA

Received 2016 September 26; revised 2017 February 13; accepted 2017 February 27; published 2017 March 29

## Abstract

We present results on the clustering properties of galaxies as a function of both stellar mass and specific star formation rate (sSFR) using data from the PRIMUS and DEEP2 galaxy redshift surveys spanning  $0.2 < z < 1.2$ . We use spectroscopic redshifts of over 100,000 galaxies covering an area of  $7.2 \text{ deg}^2$  over five separate fields on the sky, from which we calculate cosmic variance errors. We find that the galaxy clustering amplitude is as strong of a function of sSFR as of stellar mass, and that at a given sSFR, it does not significantly depend on stellar mass within the range probed here. We further find that within the star-forming population and at a given stellar mass, galaxies above the main sequence of star formation with higher sSFR are less clustered than galaxies below the main sequence with lower sSFR. We also find that within the quiescent population, galaxies with higher sSFR are less clustered than galaxies with lower sSFR, at a given stellar mass. We show that the galaxy clustering amplitude smoothly increases with both increasing stellar mass and decreasing sSFR, implying that galaxies likely evolve *across* the main sequence, not only along it, before galaxies eventually become quiescent. These results imply that the relation of stellar mass to halo mass, which connects galaxies to dark matter halos, likely depends on sSFR.

*Key words:* galaxies: evolution – galaxies: halos – galaxies: high-redshift – large-scale structure of universe

## 1. Introduction

Galaxies are thought to form in the centers of dark matter halos, regions of the universe that have collapsed under their own gravity. The observed clustering of galaxies matches well the predicted clustering of dark matter halos from  $\Lambda$ CDM cosmological numerical simulations, using various prescriptions for assigning galaxies to halos. However, it is not yet clear exactly how to map observed galaxies to dark matter halos, as it is not yet known exactly how galaxies form and evolve within these halos across cosmic time and how the dark matter halo influences the galaxy and vice versa.

Earlier galaxy clustering papers often quantified in particular the luminosity dependence of clustering, generally finding that the brightest galaxies are more clustered than fainter galaxies, with a sharp rise in the clustering amplitude above  $L^*$  (e.g., Alimi et al. 1988; Benoist et al. 1996; Norberg et al. 2001). Similar results were found to hold at higher redshift as well, to  $z \sim 1$ , when the universe was less than half its current age (e.g., Coil et al. 2006; Pollo et al. 2006; Meneux et al. 2009).

As the observed bimodality in the optical colors of galaxies became increasingly apparent (e.g., Strateva et al. 2001; Baldry et al. 2004), many authors turned toward measuring the luminosity dependence of blue star-forming and red quiescent galaxies separately (e.g., Norberg et al. 2002; Hogg et al. 2003; Coil et al. 2004b; Zehavi et al. 2005; Meneux et al. 2006). These papers showed that at a given luminosity, red galaxies are more clustered than blue, and that within each of these two broad galaxy populations, the brightest galaxies are typically more clustered than fainter galaxies. Here again these results were found to hold out to  $z \sim 1$ . However, it was also discovered at low redshift that within the red quiescent galaxy population, low-luminosity galaxies are highly clustered, likely

reflecting that they tend to be satellite galaxies in massive dark matter halos hosting galaxy clusters (Berlind et al. 2005). Some authors choose to split the galaxy population by morphology or spectral type instead of color, finding similar results, that galaxies with early-type, elliptical morphologies or early-type spectra are more clustered than late-type, spiral galaxies (e.g., Loveday et al. 1995; Madgwick et al. 2003; Li et al. 2006; de la Torre et al. 2011).

Moving beyond considering the galaxy population as having only two general types, Coil et al. (2008) used the DEEP2 galaxy redshift survey to split the  $z \sim 1$  galaxy population into finer bins in color, showing that the clustering amplitude rises within the blue star-forming population alone, as the color becomes increasingly red. They did not find any clustering difference within the red quiescent population when split by optical color. Zehavi et al. (2011) found, using the Sloan Digital Sky Survey (SDSS) at  $z \sim 0$ , that clustering depends on color within both the blue star-forming population and the red quiescent population. Using the PRIMUS galaxy redshift survey at  $z \sim 0.7$ , Skibba et al. (2014) found again that clustering depends on color within the red quiescent population (though not within the blue star-forming population). These results began to more fully flesh out how galaxy clustering depends on the star formation properties of galaxies, beyond a simple division into star-forming or quiescent, and pointed to how galaxies must evolve with time in terms of their color (from very blue to very red).

More recently, observers and theorists have moved from mapping the galaxy population in color–magnitude space to star formation rate (SFR) or specific SFR (sSFR, defined as the SFR per unit stellar mass) versus stellar mass space (e.g., Noeske et al. 2007; Speagle et al. 2014, and references therein). The latter quantities are more useful parameters as they are tied to physical processes occurring within galaxies (converting gas

into stars, the growth of a galaxy) and are less impacted by dust obscuration. They are also easier quantities for theorists to model in cosmological simulations than color and magnitude. As a result, more recently there has been a lot of work quantifying the stellar mass dependence of galaxy clustering (e.g., Li et al. 2006; Meneux et al. 2008; Wake et al. 2011; Leauthaud et al. 2012; Marulli et al. 2013). These papers typically find that the clustering amplitude is a strong positive function of stellar mass above  $M^*$  and is less dependent at lower stellar masses. This has led to many papers quantifying the relation of stellar mass to halo mass and its evolution with cosmic time (e.g., Behroozi et al. 2010; Moster et al. 2010; Leauthaud et al. 2011; Durkalec et al. 2015; Skibba et al. 2015).

While there has been substantial work on the stellar mass dependence of galaxy clustering, there have been few papers on the SFR or sSFR dependence, at either low or high redshift. In a pair of related papers, Hearin et al. (2014) and Watson et al. (2015) show that the clustering properties of SDSS galaxies divided into star-forming or quiescent at a given stellar mass are very similar whether the galaxy subsamples are defined using optical colors or sSFR. Essentially, as long as the observed bimodality in the galaxy population is used, whether the color or sSFR is used to define the bimodality does not matter in terms of the relative clustering of blue star-forming galaxies to red quiescent galaxies, perhaps not surprisingly.

Li et al. (2008) use SDSS to compare low- and high-sSFR samples within the star-forming population and find that on very small scales (less than 100 kpc) the clustering amplitude is higher for galaxies with higher sSFR. This is likely due to galaxy–galaxy tidal interactions. Heinis et al. (2009) use *GALEX* imaging of SDSS to investigate both the  $\text{NUV}-r$  and sSFR dependence of clustering, finding that the clustering amplitude increases with decreasing sSFR or redder color, where they split the star-forming population into two bins and compare with the quiescent population.

Other papers that have divided the full galaxy population more finely into multiple bins in either SFR or sSFR have typically used only angular clustering measurements, where spectroscopic redshifts are lacking for individual galaxies (Sobral et al. 2010; Lin et al. 2012; Dolley et al. 2014; Kim et al. 2015). These papers, which span  $z \sim 0.2 - 2.0$ , generally find that galaxy subsamples with higher SFR or lower sSFR have higher clustering amplitudes. Sobral et al. (2010) measure the angular clustering of  $\text{H}\alpha$  emitters at  $z \sim 0.8$  and find that clustering amplitude increases steadily with  $\text{H}\alpha$  luminosity (which is a proxy for SFR), even at a fixed  $K$ -band luminosity (which is a proxy for stellar mass). Dolley et al. (2014) measure the angular clustering of star-forming galaxies over a wide area of  $8 \text{ deg}^2$ , selecting galaxy subsamples based on IRAC/MIPS  $24 \mu\text{m}$  flux. They find that galaxies with higher  $24 \mu\text{m}$  flux (which is a proxy for SFR) have higher clustering amplitudes, though they do not investigate whether this difference may be accounted for by differences in the mean stellar mass of the samples. Kim et al. (2015) measure the angular clustering of galaxies at  $z \sim 1$  in the UKIDSS DXS survey as a function of stellar mass and sSFR. They find a steady increase in the clustering amplitude with decreasing sSFR, above a given stellar mass threshold.

Mostek et al. (2013) use the DEEP2 galaxy redshift survey at  $z \sim 1$  to measure the stellar mass, SFR, and sSFR dependence of galaxy clustering, using multiple bins in each physical

parameter. They find that within the star-forming population, clustering amplitude increases with increasing SFR and decreasing sSFR, though they find no SFR dependence for quiescent galaxies. They investigate whether the SFR dependence that is observed could be due to stellar mass and conclude that much, though not all, of the trend could be due to the known correlation between SFR and stellar mass (the star-forming “main sequence”). They also investigate small-scale clustering properties and find a clustering excess for higher-sSFR samples within both the star-forming and quiescent populations, which they attribute to galaxy–galaxy interactions.

Mostek et al. (2013) also find that star-forming galaxies above the “main sequence” of star formation are less clustered than those below, within a given stellar mass range, which points to the possibility of using clustering measurements to track the evolution of galaxies in the SFR–stellar mass plane. However, the DEEP2 sample is not large enough to further divide the galaxy population into multiple bins in SFR and stellar mass.

Here we use data from the PRIMUS and DEEP2 galaxy redshift surveys to study the dependence of galaxy clustering on stellar mass and sSFR using a sample of over 100,000 spectroscopic redshifts at  $0.2 < z < 1.2$ . Our sample spans a total of five fields, which we use to quantify errors due to cosmic variance. We use deep multiwavelength imaging in our fields to estimate stellar masses and sSFRs, from which we create multiple galaxy subsamples using cuts in both parameters. We measure cross-correlation functions (CCFs) of these galaxy subsamples with all galaxies in our survey at these redshifts, to better trace the underlying cosmic web and reduce our uncertainties.

This paper is organized as follows. In Section 2 we present the relevant spectroscopic data sets used here and describe our methodology for deriving stellar masses and sSFRs. In Section 3 we describe the various galaxy subsamples used in our clustering analysis. The methods used to perform the clustering analysis are presented in Section 4, and our results are given in Section 5. We discuss our results in Section 6 and conclude in Section 7. Throughout the paper we assume a standard  $\Lambda$ CDM model with  $\Omega_m = 0.3$ ,  $\Omega_\Lambda = 0.7$ , and  $H_0 = 72 \text{ km s}^{-1} \text{ Mpc}^{-1}$ .

## 2. Data

For this study we use data from the PRIMUS (Coil et al. 2011; Cool et al. 2013) and DEEP2 (Newman et al. 2013) galaxy spectroscopic redshift surveys. The data used here are taken from five independent fields on the sky, covering a total of  $7.2 \text{ deg}^2$ . We use the separate fields to quantify the effects of cosmic variance on the clustering properties of galaxies, as described below. Here we use data from the CDFS-SWIRE (Lonsdale et al. 2003), COSMOS (Scoville et al. 2007), Elais-S1 (ES1 Oliver et al. 2000), and XMM-LSS (Pierre et al. 2004) fields in the PRIMUS survey, as well as the Extended Groth Strip (EGS) in the DEEP2 survey. We describe the PRIMUS and DEEP2 spectroscopic surveys briefly in Sections 2.1 and 2.2, and in Section 2.3 we explain the methods we use to estimate stellar masses and SFRs in these data sets.

### 2.1. PRIMUS Redshift Survey

We use spectroscopic redshifts from the PRIMUS redshift survey to perform our clustering analysis. PRIMUS is currently

the largest faint galaxy redshift survey completed to date. The full survey covers  $\sim 9 \text{ deg}^2$  in a total of seven well-studied fields on the sky with multiwavelength imaging, including X-ray, infrared (IR), and ultraviolet (UV). The survey obtained low-resolution ( $\lambda/\Delta\lambda \sim 40$ ) spectra with the IMACS instrument (Bigelow & Dressler 2003) on the Magellan I Baade 6.5 m telescope, observing  $\sim 2500$  objects simultaneously over an area of  $0.18 \text{ deg}^2$ . PRIMUS contains a statistically complete sample of  $\sim 120,000$  robust spectroscopic redshifts to  $i_{AB} \sim 23.5$ .

Redshifts are derived by fitting a large suite of galaxy, broad-line active galactic nucleus (AGN), and stellar spectral templates to the low-resolution spectra and optical photometry (see Cool et al. 2013, for details). Objects are classified as galaxies, broad-line AGNs, or stars depending on the best  $\chi^2$  template fit. The PRIMUS spectroscopic redshifts have a precision of  $\sigma_z/(1+z) \sim 0.5\%$ . We use robust ( $z_{\text{quality}} \geq 3$ ; see Coil et al. 2011) PRIMUS redshifts between  $0.2 < z < 1.2$  in the CDFS-SWIRE, COSMOS, ES1, and XMM-LSS fields. For further details of the survey design, targeting, and data see Coil et al. (2011); for details of the data reduction, redshift confidence, and completeness see Cool et al. (2013).

The PRIMUS survey generally targeted all sources above  $i < 22.5$  and sparse-sampled  $22.5 < i < 23$  sources, so that faint galaxy sources at the flux limit would not dominate the target selection. The targeting weights were defined a priori such that a statistically complete flux-limited sample could be recreated, by tracking both the ‘‘sparse sampling’’ weight and the ‘‘density-dependent’’ weight of each object. The sparse sampling weight accounts for the fraction of sources selected at random in the 0.5 mag interval above the targeting limit in each field; it is therefore a magnitude-dependent weight. In contrast, the density-dependent weight accounts for sources in high-density areas on the plane of the sky that cannot be targeted owing to slit collisions and the number of overlapping masks observed (see Coil et al. 2011; Moustakas et al. 2013, for more details). From the full PRIMUS sample, only those targets defined as belonging to the ‘‘primary’’ sample have these well-defined targeting weights; hence, for our clustering analysis we use only ‘‘primary’’ targets.

For the clustering measurements presented here, we also include a spatially varying redshift success weight to account for changes in the observed redshift success fraction across a field (i.e., due to differences in observing conditions for different slitmasks). In the PRIMUS fields we use the `pixelize` function in `Mangle` to create these weights. We estimate the redshift success fraction by taking the ratio of robust redshift sources with  $z_{\text{quality}} \geq 3$  to all targeted sources in the field, using pixels of size  $\sim 36 \text{ arcsec}^2$ .

## 2.2. DEEP2 Redshift Survey

We also use spectroscopic redshifts from the EGS field of the DEEP2 survey (Newman et al. 2013). The DEEP2 survey was conducted with the DEIMOS spectrograph (Faber et al. 2003) on the 10 m Keck II telescope. In the EGS, the DEEP2 survey has measured  $\sim 17,000$  high-confidence redshifts ( $Q \geq 3$ ; see Newman et al. 2013) to  $R_{AB} = 24.1$ . Unlike the other DEEP2 fields, in the EGS there was no photometric redshift preselection of targets; thus, all galaxies that could be observed on slitmasks to this photometric depth were targeted. We use the Data Release 4 (DR4) catalog<sup>5</sup> and associated window

function from Newman et al. (2013). We use redshifts between  $0.2 < z < 1.2$  that have a redshift confidence greater than 95% ( $Q \geq 3$ ). We use the extended optical photometry from Matthews et al. (2013), which contains additional Canada–France–Hawaii Telescope Legacy Survey *ugriz* and the SDSS *ugriz* photometry matched to the redshift catalog. *K*-corrections, absolute  $M_B$  magnitudes, and rest-frame colors are derived from *K*-corrections (Blanton & Roweis 2007) from the optical photometry in these fields.

As in the PRIMUS fields, in the EGS we also include a spatially varying redshift success weight, which reflects the probability that a targeted source has a secure  $z_{\text{quality}} \geq 3$  redshift. For the EGS we calculate this in  $\sim 6 \text{ arcsec}^2$  pixels, as the deeper DEEP2 data allow us to use smaller pixels than in the PRIMUS fields. However, using the average of six adjacent pixels to match the  $\sim 36 \text{ arcsec}^2$  pixels used in PRIMUS does not change the resulting clustering measurements in this field.

In order to perform accurate clustering measurements, we require that all of the PRIMUS and DEEP2 sources used here are located within the area of each survey that has a well-understood spatial selection function. This ensures that any spatially dependent density differences in the surveys that are due to target selection or missing data, such as in CCD chip gaps or around bright stars, are well accounted for. In PRIMUS we require that sources fall within the observed window function area targeted with at least two slitmasks. Details of the PRIMUS spatial selection function are given in Coil et al. (2011, 2004a), and Newman et al. (2013) provide details for the DEEP2 survey.

## 2.3. Stellar Mass and sSFR Estimates

We estimate stellar masses and sSFRs by fitting the spectral energy distributions (SEDs) of our sources with population synthesis models using `iSEDfit` (Moustakas et al. 2013). `iSEDfit` is a Bayesian fitting code that compares the observed photometry for each source to a large Monte Carlo grid of SED models that span a wide range of stellar population parameters, including age, metallicity, and star formation history (SFH), to estimate the stellar mass and SFR of a galaxy. The sSFR is then simply defined as the SFR divided by the stellar mass. We use `iSEDfit` results derived from photometry spanning the UV to the near-IR IRAC bands. We assume a Chabrier (2003) initial mass function from 0.1 to  $100 M_{\odot}$  and use Bruzual & Charlot (2003) stellar population synthesis models. We assume the following priors to construct the Monte Carlo grids: uniform stellar metallicity in the range of  $0.004 < Z < 0.04$ ; Charlot & Fall (2000) dust attenuation law, with an exponential distribution of dust, ( $0.25 < \gamma < 2.0$ ); and an exponentially declining- $\tau$  ( $\phi_s(t) = (M/\tau)e^{-t/\tau}$ ) SFH with  $0.01 < \tau < 5.0$ . Stochastic bursts of star formation of varying amplitude, duration, and onset time are superimposed, allowing for a wide range of possible SFHs. While a delayed- $\tau$  model encompasses both a linearly rising ( $t/\tau \ll 1$ ) and an exponentially declining ( $t/\tau \gg 1$ ) SFH, we find no significant SFR or stellar mass offsets or trends using different SFH models for our sources at  $z < 1.2$ , and we therefore choose to use a simpler model of an exponentially declining SFH. `iSEDfit` marginalizes the full posterior probability distribution of stellar masses and SFRs over all other parameters and thus encapsulates both the uncertainties in the observations and the model parameter degeneracies. For each source we take the median stellar mass and SFR from the full probability distribution functions as the

<sup>5</sup> <http://deep.ps.uci.edu/dr4/home.html>

**Table 1**  
Galaxy Samples

Run	Name	$N_{\text{gal}}^{\text{a}}$	$z$		$\log(M_*/M_{\odot})$		$\log(\text{sSFR}/\text{yr}^{-1})$			
			Mean	Min	Mean	Max	Min	Mean	Max	
1	blue-lowz <sup>b</sup>	7,418	0.51	10.50	10.71	11.00	-11.37	-10.21	-8.25	
	red-lowz	6349	0.51	10.50	10.74	11.00	-13.08	-11.61	-10.70	
	blue-highz	6674	0.89	10.50	10.73	11.00	-10.77	-9.89	-8.11	
	red-highz	5169	0.87	10.50	10.79	11.00	-12.23	-11.09	-10.16	
2	blue1-lowz	21,600	0.52	8.50	9.73	10.50	-10.03	-9.26	-7.94	
	blue2-lowz	23,795	0.41	8.50	9.59	10.50	-11.25	-9.80	-8.75	
	red1-lowz	6797	0.56	10.10	10.76	11.60	-12.16	-11.35	-10.59	
	red2-lowz	5641	0.42	10.10	10.64	11.60	-13.32	-11.92	-11.26	
	blue1-highz	11,087	0.89	8.70	9.91	10.50	-9.68	-9.02	-7.93	
	blue2-highz	7837	0.82	8.70	9.96	10.50	-10.62	-9.58	-8.52	
	red1-highz	5372	0.92	10.10	10.97	11.60	-11.61	-10.82	-10.05	
	red2-highz	4257	0.82	10.10	10.83	11.60	-12.23	-11.41	-10.75	
3	1-lowz	4934	0.53	8.50	9.26	10.50	-9.00	-8.79	-8.00	
	2-lowz	22,744	0.47	8.50	9.53	10.50	-9.60	-9.33	-9.00	
	3-lowz	16,271	0.44	8.50	9.91	10.50	-10.60	-9.93	-9.60	
	4-lowz	5437	0.51	10.00	10.61	11.50	-11.20	-10.90	-10.60	
	5-lowz	6817	0.52	10.00	10.67	11.50	-11.80	-11.51	-11.20	
	6-lowz	3824	0.39	10.00	10.78	11.50	-12.60	-12.06	-11.80	
	1-highz	3861	0.90	9.00	9.66	11.00	-8.90	-8.66	-8.00	
	2-highz	12,770	0.87	9.00	10.04	11.00	-9.60	-9.27	-8.90	
	3-highz	6914	0.87	9.50	10.51	11.00	-10.20	-9.85	-9.60	
	4-highz	4888	0.88	10.20	10.88	11.70	-10.80	-10.49	-10.20	
	5-highz	3337	0.89	10.20	10.93	11.70	-11.20	-11.00	-10.80	
	6-highz	4109	0.84	10.20	10.93	11.70	-11.80	-11.42	-11.20	
	4	1-lowz	7067	0.49	8.50	9.12	9.50	-9.20	-8.95	-8.20
		2-lowz	10,577	0.38	8.50	9.18	9.50	-10.20	-9.48	-9.20
3-lowz		3494	0.56	9.50	9.78	10.50	-9.20	-9.02	-8.20	
4-lowz		19,817	0.49	9.50	9.96	10.50	-10.20	-9.65	-9.20	
5-lowz		5698	0.45	9.50	10.15	10.50	-11.20	-10.65	-10.20	
6-lowz		3618	0.42	9.50	10.20	10.50	-12.20	-11.59	-11.20	
7-lowz		3870	0.53	10.50	10.74	11.50	-10.20	-9.85	-9.20	
8-lowz		5875	0.53	10.50	10.80	11.50	-11.20	-10.68	-10.20	
9-lowz		6913	0.51	10.50	10.86	11.50	-12.20	-11.67	-11.20	
1-highz		2291	0.82	8.50	9.31	9.50	-9.20	-8.76	-8.20	
2-highz		6232	0.90	9.50	9.89	10.50	-9.20	-8.94	-8.20	
3-highz		9674	0.85	9.50	10.13	10.50	-10.20	-9.53	-9.20	
4-highz		944	0.79	9.50	10.36	10.50	-11.20	-10.61	-10.20	
5-highz		5964	0.91	10.50	10.80	11.50	-10.20	-9.80	-9.20	
6-highz	7295	0.89	10.50	10.94	11.50	-11.20	-10.70	-10.20		
7-highz	3949	0.84	10.50	10.95	11.50	-12.10	-11.44	-11.20		

**Notes.**

<sup>a</sup> This is the weighted number of galaxies in each sample; weights are discussed in Section 2.

<sup>b</sup> The “low- $z$ ” samples span  $0.2 < z < 0.7$ , while the “high- $z$ ” samples span  $0.7 < z < 1.2$ .

best estimate of the stellar mass and SFR. The median uncertainties on the log stellar mass and SFR are 0.08 and 0.2 dex, respectively. While the systematic errors on the stellar mass and SFR estimates may be larger than the statistical errors, our concern in this paper is how the relative bias scales with stellar mass and sSFR. So long as systematic errors in determining these parameters do not correlate with large-scale density on scales  $> 1 h^{-1}$  Mpc, then our conclusions are robust to these systematics.

### 3. Galaxy Samples

The goal of this paper is to quantify the dependence of galaxy clustering at intermediate redshift on stellar mass and sSFR. To facilitate this, we created various galaxy samples from the full galaxy population, which is defined as all galaxies with robust redshifts (as described above) at  $0.2 < z < 1.2$ .

We create galaxy samples four times, which we call four “runs,” using different cuts in stellar mass and sSFR for each run. We always create galaxy samples in two redshift intervals for each run:  $0.2 < z < 0.7$  and  $0.7 < z < 1.2$ .

We identify star-forming and quiescent galaxies based on their location in the SFR versus stellar mass plane, using an evolving linear relation that traces the minimum of the bimodal galaxy distribution in PRIMUS:

$$\log(\text{SFR}) = -1.29 + 0.65(\log M_* - 10) + 1.33(z - 0.1), \quad (1)$$

where SFR has units of  $\mathcal{M}_{\odot} \text{ yr}^{-1}$  and  $M_*$  has units of  $M_{\odot}$ . The slope of this line is defined by the slope of the star-forming main sequence (e.g., Noeske et al. 2007) as measured in the PRIMUS data set using `iSEDfit` SFR and stellar mass estimates. Each galaxy is classified as star-forming or quiescent

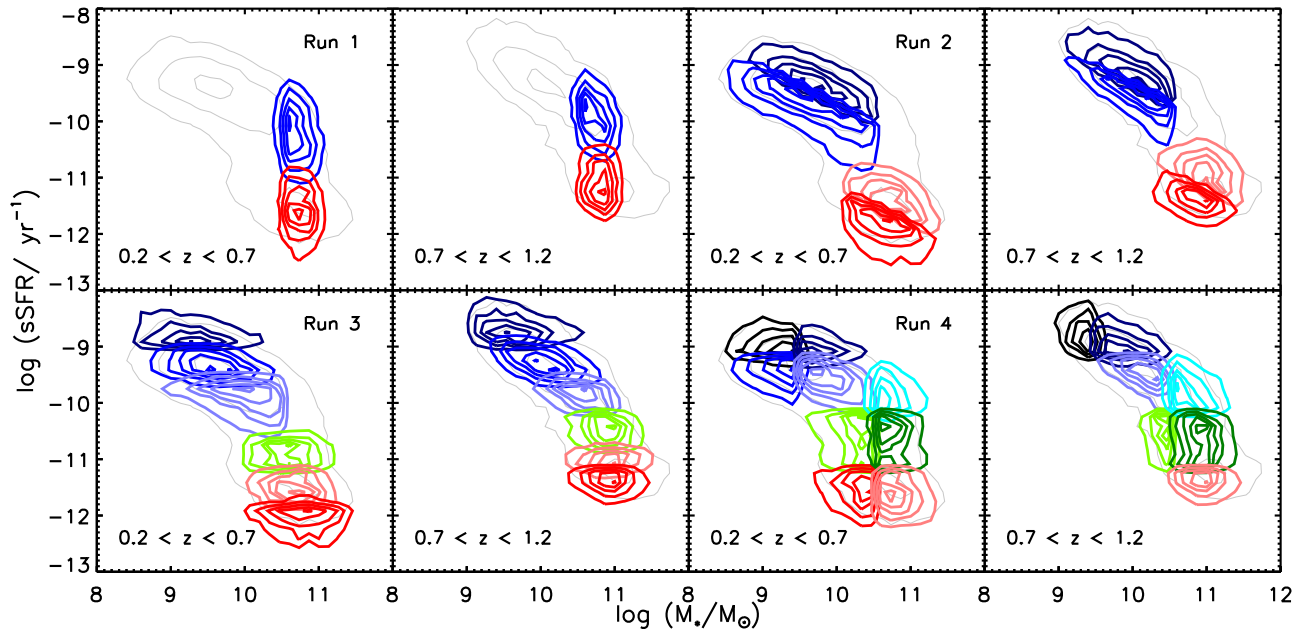


**Figure 1.** sSFR vs. stellar mass for the various galaxy samples used in this paper. We divided the full galaxy sample into four “runs,” each with various galaxy samples defined by cuts in stellar mass and sSFR, at both lower redshift ( $0.2 < z < 0.7$ ) and higher redshift ( $0.7 < z < 1.2$ ). Light-gray contours show the full galaxy population in the relevant redshift interval, while colored contours show the various galaxy samples used in each of the runs for our clustering analysis. The justification for the different runs is given in the text.

based on whether it lies above or below the cut defined by Equation (1), evaluated at the redshift of the galaxy. Figure 2 of Bertl et al. (2016) shows the distribution of PRIMUS galaxies in the SFR–stellar mass plane in bins of redshift, along with the location of this cut.

The details of the various samples created here for each run are given in Table 1, and the location of the galaxy samples in the sSFR versus stellar mass plane are shown in Figure 1. The *i*- and *R*-band selection limits used in the PRIMUS and DEEP2 redshift surveys correspond to  $\sim 4000$  Å rest-frame selection at  $z \sim 0.7$ , such that galaxies with higher sSFR (i.e., star-forming galaxies) are included in our sample at lower stellar masses than quiescent galaxies with lower sSFR. This can clearly be seen by the lack of galaxies in the lower left regions in Figure 1.

For the samples described below, the lower-redshift samples in the first run are stellar mass limited, in that all galaxies in these samples are above the stellar mass completeness limits of the PRIMUS survey (Moustakas et al. 2013). This facilitates comparisons with theoretical models that required stellar-mass-complete samples. The rest of the samples are flux limited. This is required in order to probe a wide enough range in both stellar mass and sSFR for the purposes of investigating the joint clustering dependence on these properties. These samples are useful for quantifying the relative clustering dependence but should not be interpreted as being complete to all stellar masses and sSFR values at the mean values of each sample.

For the first run, we are interested in comparing star-forming and quiescent galaxies at the same stellar mass. Therefore, we restrict the stellar mass range to  $10.5 < \log(M_*/M_\odot) < 11.0$  and create two galaxy samples in each redshift range using Equation (1). These samples are shown in the upper left panels of Figure 1 labeled “Run 1,” and we will additionally refer to this run below in the text as the “star-forming/quiescent split” run. This run allows us to compare star-forming and quiescent galaxies at similar stellar masses (the mean stellar masses of

these samples differ by only  $\sim 0.03$ – $0.06$  dex, as seen in Table 1). As stated above, the lower-redshift samples in this run are stellar mass complete.

For the second run, we are interested in comparing galaxies of higher or lower sSFR within the star-forming and quiescent populations separately. In this run we are not concerned with comparing the clustering properties of star-forming galaxies with those of quiescent galaxies; therefore, we use wider stellar mass ranges than in run 1, and we did not require the same stellar mass ranges for the star-forming and quiescent populations. Here we choose samples that effectively split the star-forming population into those galaxies above and below the main sequence of star formation, and within the quiescent population into those galaxies that are higher sSFR than those that are more quiescent. We refer to this run below in the text as the “main-sequence split” run. Within the star-forming population we require the stellar mass to be within  $8.5 < \log(M_*/M_\odot) < 10.5$  and use the following cuts:

$$\log(\text{sSFR}) + 0.65(\log M_* - 10) > -9.715, \quad (2)$$

$$\log(\text{sSFR}) + 0.65(\log M_* - 10) > -9.365, \quad (3)$$

at  $0.2 < z < 0.7$  and  $0.7 < z < 1.2$ , respectively. Within the quiescent population we restrict the mass range to  $10.1 < \log(M_*/M_\odot) < 11.6$  and use the following cuts:

$$\log(\text{sSFR}) + 0.65(\log M_* - 10.5) > -11.512, \quad (4)$$

$$\log(\text{sSFR}) + 0.65(\log M_* - 10.5) > -10.937, \quad (5)$$

at  $0.2 < z < 0.7$  and  $0.7 < z < 1.2$ , respectively.

We also ran but do not show here more simple divisions of the star-forming and quiescent populations using a strict cut in sSFR. We find very similar results to using the cuts above that include the stellar-mass-dependent tilt in the star-forming main sequence (which is derived here for our PRIMUS and DEEP2 sample, using our stellar mass and sSFR estimates).

For the third run, we use strict cuts in sSFR to split the galaxy sample into bins of sSFR, allowing for different stellar mass ranges in the star-forming and quiescent populations. We call this run the “sSFR cuts” run. For this run at  $0.2 < z < 0.7$  within the star-forming population we restrict the stellar mass range to be within  $8.5 < \log(M_*/M_\odot) < 10.5$  and use cuts in  $\log(\text{sSFR}/\text{yr}^{-1}) = -9.0$  and  $-9.6$ . Within the quiescent population we restrict the stellar mass range to be within  $10.0 < \log(M_*/M_\odot) < 11.5$  and use cuts in  $\log(\text{sSFR}/\text{yr}^{-1}) = -11.2$  and  $-11.8$ . For the higher redshift range,  $0.7 < z < 1.2$ , within the star-forming population we restrict the stellar mass range to be within  $9.0 < \log(M_*/M_\odot) < 11.0$  and use cuts in  $\log(\text{sSFR}/\text{yr}^{-1}) = -9.0$  and  $-9.6$ . Within the quiescent population we restrict the stellar mass range to be within  $10.2 < \log(M_*/M_\odot) < 11.7$  and use cuts in  $\log(\text{sSFR}/\text{yr}^{-1}) = -10.8$  and  $-11.2$ . This run effectively allows us to divide both the star-forming and quiescent populations in three samples each, based on sSFR.

For the fourth and last run, we are interested in creating samples with either the same sSFR and different stellar mass or the same stellar mass and different sSFR, to investigate the dependence of galaxy clustering on one parameter while holding the other parameter fixed. This run is used solely when measuring the relative bias between galaxy samples in Section 5.2 below. At  $0.2 < z < 0.7$  we define a total of nine samples and at  $0.7 < z < 1.2$  we define a total of seven samples based on stellar mass cuts at  $\log(M_*/M_\odot) = 9.5, 10.5,$  and  $11.5$  and  $\log(\text{sSFR}/\text{yr}^{-1}) = 9.2, 10.2,$  and  $11.2$ . The various samples are shown in the lower right panels of Figure 1, and the parameters of each sample are listed in Table 1.

Additionally, as discussed below, we employ both auto-correlation function (ACF) and CCF measurements in our analysis. The advantage of cross-correlation measurements is that it allows us to use the full galaxy population, without making cuts on stellar mass or sSFR, to trace the cosmic web of large-scale structure with more precision than is possible using smaller galaxy samples. For these CCF measurements, we create a “tracer” galaxy sample, which is simply defined as all galaxies in the full sample in the relevant redshift range. The “tracer” sample contains 69,720 galaxies at  $0.2 < z < 0.7$  and 37,721 galaxies at  $0.7 < z < 1.2$ . We then cross-correlate this “tracer” galaxy sample with the various samples defined above.

#### 4. Methods

We measure the spatial distribution of galaxies using the two-point correlation function, which quantifies the excess probability above Poisson of finding two sources with a given physical separation. While most galaxy clustering studies measure the ACF of the galaxy subsample of interest, here we measure both the ACF directly and also the CCF of the galaxy subsample of interest with a tracer galaxy sample, from which we then infer the ACF of the subsample of interest alone. The main advantage of this method is that it reduces the error bars on the ACF for small galaxy subsamples, as the tracer sample has a much higher space density and is used to more fully trace the underlying large-scale structure. Details of how we perform these measurements and measure both absolute and relative biases are given below.

##### 4.1. Measuring the Two-point Correlation Function

The two-point correlation function  $\xi(r)$  is defined as a measure of the excess probability  $dP$  (above that for an unclustered distribution) of finding a galaxy in a volume element  $dV$  at a separation  $r$  from another randomly chosen galaxy,

$$dP = n[1 + \xi(r)]dV, \quad (6)$$

where  $n$  is the mean number density of the galaxy sample in question (Peebles 1980).

For each galaxy subsample we construct a randomly distributed catalog with the same overall sky coverage and redshift distribution as the data. The random catalog includes information on the redshift success fraction, as discussed above. We then measure the two-point correlation function using the Landy & Szalay (1993) estimator,

$$\xi = \frac{1}{RR} \left[ DD \left( \frac{n_R}{n_D} \right)^2 - 2DR \left( \frac{n_R}{n_D} \right) + RR \right], \quad (7)$$

where  $DD$ ,  $DR$ , and  $RR$  are weighted counts of pairs of galaxies (as a function of separation) in the data–data, data–random, and random–random catalogs, and  $n_D$  and  $n_R$  are the mean weighted number densities of galaxies in the data and random catalogs. Weights are used to account for target selection in the PRIMUS sample (see Section 2); by applying these weights, we are able to create a statistically complete sample that is not subject to spatial biases. In the DEEP2 fields the weights are included in the spatial selection function, which we use to generate the random catalogs, such that galaxies have unity weight. In order to determine the radial function of the random catalogs, we used a high-pass filter in combination with boxcar smoothing of the redshift distribution of the galaxies in each field. This preserves the shape due to the selection function of the survey while removing deviations due to large-scale structure.

The ACF measures the clustering of a single sample, where the two sources are from the same sample, while the CCF measures the clustering of one type of source, taken from one sample, around that of another type of source, taken from a second sample. Here we measure the CCF of the galaxy subsample of interest with the “tracer” galaxy sample, which is all galaxies with robust redshifts in the redshift range of interest. To measure the CCF between two galaxy samples, we measure the observed number of galaxies from a given sample around each galaxy in the other sample as a function of distance, divided by the expected number of galaxies for a random distribution. We use the Davis & Peebles (1983) estimator:

$$\xi(r) = \frac{D_1 D_2(r)}{D_1 R(r)} - 1, \quad (8)$$

where  $D_1 D_2(r)$  is the sum of the weighted pairs of galaxies between the two samples and  $D_1 R(r)$  is the sum of the weighted galaxy–random pairs, both as a function of separation. Here again weights are used to account for target selection in the PRIMUS survey and the spatial selection function in the DEEP2 survey.

Peculiar velocities distort  $\xi(r)$  measurements along the line of sight. We therefore measure  $\xi(r)$  in two dimensions,

$\xi(r_p, \pi)$ , where  $r_p$  is the separation perpendicular to the line of sight, which is unaffected by peculiar velocities, and  $\pi$  is the separation along the line of sight. Integrating  $\xi(r_p, \pi)$  along the  $\pi$  dimension leads to a statistic that is independent of redshift space distortions, the projected correlation function:

$$w_p(r_p) = 2 \int_0^\infty d\pi \xi(r_p, \pi), \quad (9)$$

$$\approx 2 \int_0^{\pi_{\max}} d\pi \xi(r_p, \pi), \quad (10)$$

where  $\pi_{\max}$  is the maximum  $\pi$  separation to which we integrate. As the signal-to-noise ratio of  $\xi(r_p, \pi)$  declines quickly for large values of  $\pi$ , we measure the projected correlation function by integrating to a given  $\pi_{\max}$  to limit shot noise. We use a limit of  $\pi_{\max} = 40 h^{-1} \text{ Mpc}$  in both the PRIMUS and DEEP2 surveys.

#### 4.2. Jackknife Error Estimation

We estimate the uncertainty in our measurements using jackknife resampling of the data. For reasonably large surveys like PRIMUS and DEEP2 jackknife errors are generally similar to the cosmic variance errors in  $w_p$  derived from simulated mock catalogs (e.g., Coil et al. 2008; Skibba et al. 2014). We use 11 jackknife samples across our five fields, where we have spatially subdivided the larger fields (CDFS-SWIRE and XMM-LSS) into two or more subfields along lines of constant right ascension and declination such that the resulting subsamples probe roughly similar volumes and cover an area on the sky approximately equal to  $\sim 1 \text{ deg}^2$ .

The uncertainty in  $w_p$  is estimated by calculating the projected correlation function using each jackknife sample. From this collection of  $w_p$  estimates we calculate the variance in the projected correlation function,

$$\sigma_{w_p}^2(r_p) = \frac{N-1}{N} \sum_j (w_p(r_p) - \hat{w}_j(r_p))^2, \quad (11)$$

where  $N$  is the number of jackknife samples,  $j$  indexes each jackknife sample, and  $\hat{w}_j(r_p)$  is the projected correlation function computed for a given jackknife sample. By measuring the projected correlation function using multiple fields across the sky, the jackknife resampling estimates the uncertainty on our measurements due to cosmic variance.

#### 4.3. Inferring the Auto-correlation Function

In addition to directly measuring the ACF of the various galaxy subsamples, we also infer the ACF of these subsamples using the measured CCF with the tracer sample. To do this, we also measure the ACF of the tracer sample in the same volume as the galaxy subsample of interest. We integrate all ACFs and CCFs to the same  $\pi_{\max}$  limit. We then infer the ACF of the galaxy subsample of interest using

$$w_{\text{GG}}(r_p) = \frac{w_{\text{GT}}^2(r_p)}{w_{\text{TT}}(r_p)}, \quad (12)$$

where  $w_{\text{GG}}$  is the projected ACF of the galaxy subsample of interest,  $w_{\text{GT}}$  is the projected galaxy-tracer CCF, and  $w_{\text{TT}}$  is the projected tracer ACF. Implicit is the assumption that the spatial distributions of the galaxies of interest and the tracer galaxies are linearly related to the underlying dark matter spatial

distribution (i.e., that the bias is linear; see Section 4.5) and that galaxies of interest and the tracer galaxies are well mixed within dark matter halos. To validate this assumption, below we compare the directly measured ACF of both star-forming and quiescent galaxies with the ACF inferred from the CCF and find excellent agreement on both small and large projected scales, well within the errors.

#### 4.4. Power-law Fits

The two-point correlation function can roughly be fit by a power law, with  $\xi(r) = (r/r_0)^\gamma$ , where the scale factor  $r_0$  is the scale at which there is unity excess probability and  $\xi = 1$ . An analytic form can then be fit to  $w_p(r_p)$ :

$$w_p(r_p) = r_p \left( \frac{r_0}{r_p} \right)^\gamma \frac{\Gamma\left(\frac{1}{2}\right)\Gamma\left(\frac{\gamma-1}{2}\right)}{\Gamma\left(\frac{\gamma}{2}\right)}, \quad (13)$$

where  $\Gamma$  is the gamma function. We fit this analytic function to our clustering measurements in the approximately linear regime of  $1 h^{-1} \text{ Mpc} < r_p < 10 h^{-1} \text{ Mpc}$ . On larger scales the size of our fields limits the number of pair counts, which artificially lowers the measured correlation function and leads to large statistical fluctuations. While power-law fits can also be performed on smaller scales, here we present power-law fits only on scales of  $1 h^{-1} \text{ Mpc} < r_p < 10 h^{-1} \text{ Mpc}$  and present bias analyses on both small and large scales.

#### 4.5. Absolute and Relative Bias Measurements

We use the measured projected correlation function to estimate the absolute bias, or dark matter bias, of the various galaxy subsamples. The absolute bias  $b$  measures the relative clustering strength of the galaxy subsample to that of dark matter particles. We estimate this bias at the median redshift of each galaxy subsample using the publicly available code of Smith et al. (2003). We integrate the dark matter correlation function to a  $\pi_{\max} = 40 h^{-1} \text{ Mpc}$  and then calculate the bias as

$$b = \sqrt{\frac{w_{\text{G}}}{w_{\text{DM}}}}, \quad (14)$$

where  $w_{\text{G}}$  is the galaxy ACF and  $w_{\text{DM}}$  is the dark matter ACF on scales of  $1 h^{-1} \text{ Mpc} < r_p < 10 h^{-1} \text{ Mpc}$ . We determine  $w_{\text{DM}}$  at the mean redshift of the relevant galaxy sample. When comparing the clustering of different samples—particularly with other published papers—it is useful to compare the bias values instead of the clustering scale lengths, as the bias accounts for differences in the median redshift of each sample and further does not assume that  $\xi$  is a power law. The clustering scale length is also covariant with the slope of the power law, such that ideally the slopes should be fixed when comparing results for different samples. It is therefore preferred to compare the bias values.

Additionally, the relative bias between two galaxy subsamples is defined as the square root of the ratio of their respective projected correlation functions. This allows for a simple comparison of the clustering strength of two samples and is akin to comparing their absolute bias (relative to dark matter) values. We estimate the relative bias on two scales:  $0.1 < r_p < 10 h^{-1} \text{ Mpc}$  (which we refer to as the “one-halo” or “small-scale” relative bias) and  $1 h^{-1} \text{ Mpc} < r_p < 10 h^{-1} \text{ Mpc}$

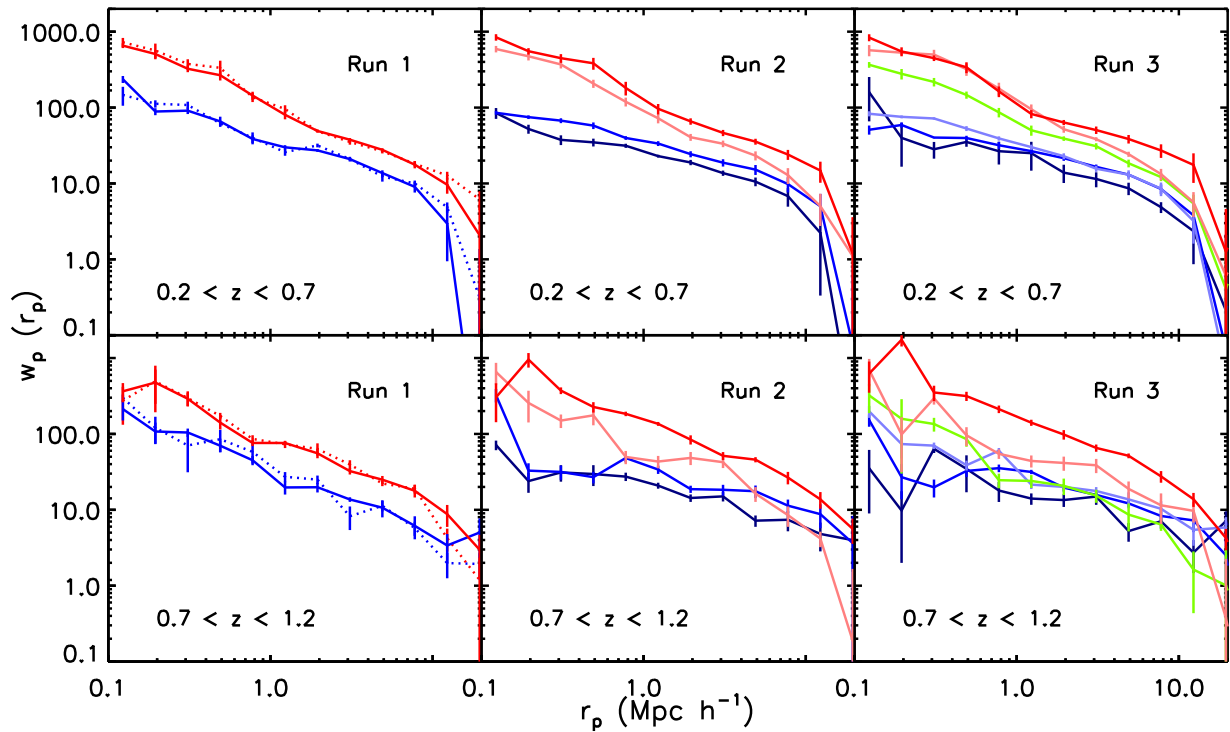


**Figure 2.**  $w_p(r_p)$  for the galaxy samples in runs 1 (star-forming/quiescent split), 2 (main-sequence split), and 3 (sSFR cuts). The colors of each sample correspond to the colors shown in Figure 1. The upper row shows  $w_p(r_p)$  for the redshift range  $0.2 < z < 0.7$ , and the lower row shows  $w_p(r_p)$  for  $0.7 < z < 1.2$ . In the left column, for run 1, the dotted lines show  $w_p(r_p)$  derived from autocorrelation function measurements, while the solid lines show  $w_p(r_p)$  derived from CCF measurements. Given the excellent agreement between them, we utilize  $w_p(r_p)$  derived from CCF measurements only for all results in this paper.

**Table 2**  
 $w_p$  Measurements for Run 1 (“Star-forming/Quiescent Split”)

$r_p$	blue-lowz	red-lowz	blue-highz	red-highz
0.12	235.63 (24.73)	655.07 (46.46)	212.64 (62.31)	364.58 (103.23)
0.20	88.64 (9.29)	508.59 (62.78)	107.62 (33.29)	475.78 (226.77)
0.31	91.07 (8.94)	324.85 (32.43)	104.45 (13.16)	290.76 (58.29)
0.49	65.70 (10.07)	266.88 (39.35)	70.03 (12.42)	140.93 (26.38)
0.78	38.60 (4.47)	144.27 (17.54)	44.97 (6.29)	76.02 (6.84)
1.23	29.93 (2.00)	80.25 (10.30)	19.72 (3.85)	75.96 (4.54)
1.95	27.27 (1.19)	49.16 (2.28)	19.84 (2.90)	55.59 (7.84)
3.09	20.95 (1.49)	37.69 (1.94)	13.68 (0.94)	32.37 (3.21)
4.90	13.71 (1.17)	27.70 (1.39)	10.67 (2.72)	24.94 (2.97)
7.76	9.03 (1.45)	17.69 (1.89)	6.15 (2.07)	17.82 (3.29)
12.30	2.96 (2.02)	9.61 (2.28)	3.39 (1.41)	8.77 (2.82)
19.50	0.00 (0.46)	2.08 (3.21)	5.02 (2.69)	2.98 (1.70)

(which we refer to as the “two-halo” or “large-scale” relative bias). We use the ratio of the CCFs to measure the relative bias between two galaxy subsamples. Below we present the mean and  $1\sigma$  uncertainty of the relative bias across the jackknife samples when comparing two samples.

## 5. Results

In this section we present the two-point correlation functions of the various galaxy samples defined by cuts in stellar mass and sSFR, along with the dependence of the absolute bias on these parameters. We also investigate how the relative bias between galaxy samples depends on stellar mass and sSFR, and we show that the dependence on sSFR is stronger than the dependence on stellar mass.

### 5.1. $w_p(r_p)$ and Absolute Bias of Galaxy Samples

Figure 2 shows the two-point correlation function of the galaxy samples for runs 1, 2, and 3. For run 1 (“star-forming/quiescent split”), where we divide the galaxy population into star-forming versus quiescent for a limited stellar mass range, we show both the directly measured ACF (dotted lines) and the inferred ACF derived using the CCF with the tracer galaxy sample (solid lines). The excellent agreement between these demonstrates that the CCF can be used to robustly recover the ACF. While the CCF can result in an artificially low  $w_p$  measurement on large scales (as seen in the upper left panel of Figure 2), the resulting bias measurement decreases by only 1%; this 1% systematic is well worth the substantially reduced cosmic variance jackknife errors that are derived using the CCF. Tables 2 and 3 list the  $w_p$  measurements for the samples

**Table 3**  
 $w_p$  Measurements for Run 2 (“Main-sequence Split”)

$r_p$	blue1-lowz	blue2-lowz	red1-lowz	red2-lowz	blue1-highz	blue2-highz	red1-highz	red2-highz
0.12	84.81 (13.83)	85.36 (4.98)	591.45 (57.97)	843.65 (82.71)	71.36 (10.34)	325.09 (65.39)	655.14 (209.32)	303.74 (160.99)
0.20	52.27 (7.09)	74.84 (4.15)	474.33 (56.61)	552.70 (53.36)	23.89 (7.14)	32.84 (8.22)	256.24 (114.53)	955.32 (207.93)
0.31	37.56 (5.52)	67.27 (4.98)	370.36 (42.74)	447.45 (58.80)	31.10 (7.61)	31.56 (6.72)	149.96 (30.34)	372.66 (37.84)
0.49	34.80 (4.10)	57.87 (5.78)	207.14 (25.54)	383.22 (68.26)	29.64 (9.09)	26.93 (4.68)	175.59 (45.73)	226.58 (35.44)
0.78	31.39 (1.96)	39.77 (2.21)	119.25 (15.88)	181.31 (37.13)	27.40 (3.45)	48.13 (5.96)	49.80 (9.84)	184.03 (12.55)
1.23	22.92 (0.98)	33.59 (2.45)	72.25 (10.32)	96.36 (15.08)	20.85 (1.88)	33.92 (4.23)	43.28 (8.03)	135.78 (7.98)
1.95	18.91 (1.52)	24.34 (2.24)	40.65 (4.26)	65.76 (6.37)	14.31 (1.62)	18.73 (2.05)	48.32 (9.46)	84.11 (11.65)
3.09	13.69 (1.10)	18.77 (2.07)	33.37 (3.31)	46.40 (4.38)	15.01 (2.13)	18.36 (2.99)	42.43 (6.92)	51.47 (6.11)
4.90	10.57 (1.38)	15.23 (2.28)	23.27 (3.16)	35.62 (3.19)	7.19 (1.22)	17.58 (3.31)	16.32 (3.62)	45.78 (3.58)
7.76	6.80 (1.86)	9.82 (2.22)	12.88 (3.02)	24.07 (3.62)	7.39 (2.18)	11.34 (2.30)	8.52 (2.55)	26.61 (4.98)
12.30	2.23 (1.90)	5.02 (2.26)	5.04 (2.28)	14.79 (4.58)	4.81 (1.98)	8.77 (3.05)	4.19 (0.97)	13.74 (3.40)
19.50	0.01 (0.81)	0.07 (0.52)	1.10 (2.49)	1.19 (2.41)	3.98 (2.46)	3.64 (4.67)	0.19 (1.48)	5.60 (2.05)

**Table 4**  
Power-law and Bias Measurements<sup>a</sup>

Run	Name	$r_0$	$\gamma$	Bias
1	blue-lowz	$3.63 \pm 0.14$	$1.57 \pm 0.05$	$1.23 \pm 0.08$
	red-lowz	$5.96 \pm 0.20$	$1.82 \pm 0.11$	$1.75 \pm 0.04$
	blue-highz	$2.79 \pm 0.35$	$1.53 \pm 0.14$	$1.23 \pm 0.08$
	red-highz	$5.88 \pm 0.21$	$1.82 \pm 0.07$	$2.04 \pm 0.08$
2	blue1-lowz	$3.02 \pm 0.14$	$1.60 \pm 0.10$	$1.06 \pm 0.06$
	blue2-lowz	$3.76 \pm 0.16$	$1.62 \pm 0.08$	$1.18 \pm 0.08$
	red1-lowz	$5.46 \pm 0.32$	$1.89 \pm 0.15$	$1.64 \pm 0.07$
	red2-lowz	$6.82 \pm 0.39$	$1.75 \pm 0.09$	$1.90 \pm 0.06$
	blue1-highz	$2.76 \pm 0.12$	$1.58 \pm 0.11$	$1.19 \pm 0.12$
	blue2-highz	$3.56 \pm 0.34$	$1.55 \pm 0.13$	$1.45 \pm 0.16$
	red1-highz	$4.92 \pm 0.55$	$1.58 \pm 0.06$	$1.80 \pm 0.29$
	red2-highz	$7.60 \pm 0.41$	$1.91 \pm 0.10$	$2.56 \pm 0.13$
3	1-lowz	$3.11 \pm 0.69$	$1.86 \pm 0.27$	$0.97 \pm 0.04$
	2-lowz	$3.27 \pm 0.20$	$1.56 \pm 0.05$	$1.13 \pm 0.08$
	3-lowz	$3.55 \pm 0.18$	$1.66 \pm 0.08$	$1.13 \pm 0.06$
	4-lowz	$4.88 \pm 0.35$	$1.69 \pm 0.09$	$1.48 \pm 0.07$
	5-lowz	$5.92 \pm 0.17$	$2.04 \pm 0.15$	$1.74 \pm 0.13$
	6-lowz	$6.67 \pm 0.42$	$1.57 \pm 0.11$	$1.90 \pm 0.15$
	1-highz	$2.04 \pm 0.21$	$1.41 \pm 0.06$	$1.11 \pm 0.18$
	2-highz	$3.57 \pm 0.13$	$1.73 \pm 0.11$	$1.35 \pm 0.05$
	3-highz	$2.54 \pm 0.45$	$1.36 \pm 0.12$	$1.37 \pm 0.16$
	4-highz	$3.19 \pm 0.40$	$1.66 \pm 0.17$	$1.25 \pm 0.06$
	5-highz	$4.75 \pm 0.54$	$1.55 \pm 0.13$	$1.80 \pm 0.17$
	6-highz	$8.29 \pm 0.38$	$1.81 \pm 0.08$	$2.73 \pm 0.10$

**Note.**

<sup>a</sup> These measurements are made on scales of  $1 < r_p < 10 h^{-1} \text{Mpc}$ .

in runs 1 and 2, with the jackknife errors given in parentheses. Table 4 lists the power-law fits to the  $w_p(r_p)$  results shown in Figure 2, along with the absolute bias of each sample. We focus in this section on results from runs 1, 2, and 3 for clarity; run 4 is used below in Section 5.2, where we present relative bias results.

The clustering results from run 1 (“star-forming/quiescent split”) clearly show that at a similar stellar mass, quiescent galaxies are substantially more clustered than star-forming galaxies. Both the slope and correlation scale length are higher for the quiescent galaxy sample, in both redshift ranges. In run 2 (“main-sequence split”) we further divide both the star-forming and quiescent populations by sSFR, or more precisely, whether they are above or below the “main sequence” of star formation or a similarly sloped ridge in the quiescent

population, and we find here that, again at a given stellar mass, galaxies above the main sequence are less clustered than galaxies below the main sequence. Within the quiescent population, galaxies with higher sSFR are also less clustered than galaxies with lower sSFR. The slope of  $w_p(r_p)$  does not vary substantially within either the star-forming or quiescent populations, but at least at  $0.2 < z < 0.7$  where we have smaller error bars, there is a clear change in the slope between the star-forming and quiescent populations, as seen in run 1. We do note, however, that the mean stellar mass varies by  $\sim 1$  dex in run 2 between the star-forming and quiescent populations; the difference is much smaller in run 1.

In run 3 (“sSFR cuts”) we split the full galaxy population into six bins in sSFR, allowing the mean stellar mass to change as needed to create large galaxy samples (here again the difference is  $\sim 1$  dex between the star-forming and quiescent populations). Here we find that both the clustering scale length and slope generally increase with decreasing sSFR. As seen in Figure 2, within the quiescent population in run 3 at  $0.2 < z < 0.7$  (upper right panel) there is not a difference in the clustering properties on scales  $0.1 < r_p < 10 h^{-1} \text{Mpc}$ , but there is a difference on scales  $1 h^{-1} \text{Mpc} < r_p < 10 h^{-1} \text{Mpc}$ . At  $0.7 < z < 1.2$  there is a difference within the quiescent population on all scales, though the error bars are larger in our higher-redshift bin.

In Figure 3 we show the dependence of the large-scale bias, measured on scales  $1 h^{-1} \text{Mpc} < r_p < 10 h^{-1} \text{Mpc}$ , on stellar mass (left panels) and sSFR (right panels). We show results for galaxy samples in runs 2 (“main-sequence split”; top row) and 3 (“sSFR cuts”; bottom row) in this figure. While there is a general increase in the bias with increasing stellar mass, there are specific samples where the bias is not necessarily higher at higher stellar mass. As shown in the right panels, however, there is a clear steady increase in the bias with decreasing sSFR, such that the trend is monotonic with sSFR. We show results for both redshift ranges overlaid and note that within the errors, at a given stellar mass the bias does not show any redshift dependence, but at a given sSFR the bias at higher redshift is higher than the bias at lower redshift (i.e., the diamonds lie above the crosses in the left column of Figure 3).

As the clustering of dark matter particles increases with time, the bias between a galaxy population and dark matter particles generally decreases over time. Therefore, one would assume that the absolute bias at a given galaxy property should be higher at higher redshift. However, both the stellar mass and sSFR change with time for individual galaxies, and the sSFR of

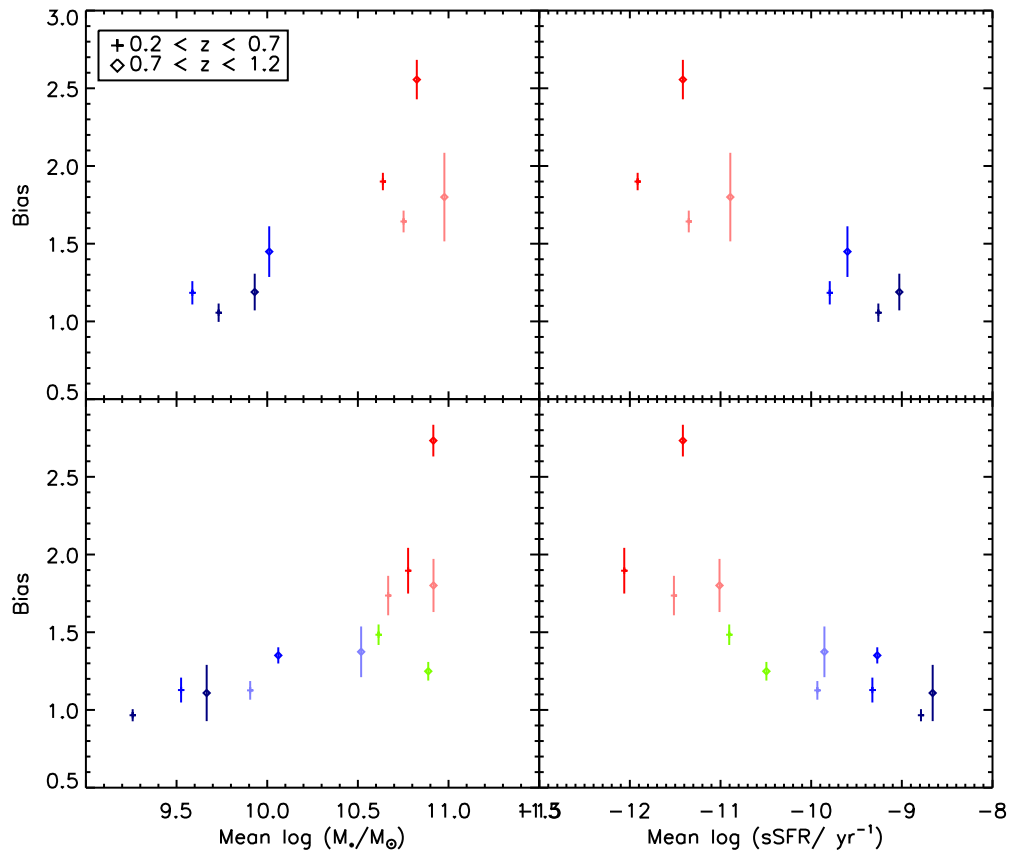


**Figure 3.** Absolute bias on scales  $1 < r_p < 10 h^{-1} \text{ Mpc}$  of each galaxy sample in runs 2 (“main-sequence split”) and 3 (“sSFR cuts”). The left column shows the bias as a function of sSFR, and the right column shows the bias as a function of stellar mass. The colors of each sample correspond to the colors shown in Figure 1.

a galaxy changes more between  $z \sim 0.9$  and  $z \sim 0.5$  than the stellar mass at  $\log(M_*/M_\odot) = 10.5$  (corresponding to the mean stellar mass probed here; e.g., Moustakas et al. 2013; Madau & Dickinson 2014). We return to this point in the discussion section below.

In Figure 4 we show with colored circles the absolute bias of various galaxy samples from runs 2 and 3 as a function of stellar mass on the  $x$ -axis and sSFR on the  $y$ -axis. The light-gray contours show the full galaxy population in our sample in the redshift range of interest. This figure allows one to clearly see how the bias is changing as a function of sSFR at a given stellar mass, within both the star-forming and quiescent populations. Generally, we find that the bias increases toward the lower right of this figure, at higher stellar mass and lower sSFR. We return in the discussion section below to how galaxies likely evolve in this plane.

### 5.2. Relative Bias between Galaxy Samples

We also quantify how the relative bias between two galaxy samples depends on both stellar mass and sSFR. The relative bias between two galaxy samples can have smaller errors than a direct comparison of the absolute bias values, as to first order cosmic variance effects will cancel when comparing the clustering of two galaxy samples in the same volume. We may therefore be able to obtain more significant dependences on how the relative bias depends on stellar mass and sSFR than quantifying only the absolute bias dependence on these parameters.

The relative bias between various galaxy subsamples from runs 2, 3, and 4 is listed in Table 5. We quantify the relative bias on two scales: the “one-halo” scale of  $0.1 < r_p < 10 h^{-1} \text{ Mpc}$  and the “two-halo” scale of  $1 h^{-1} \text{ Mpc} < r_p < 10 h^{-1} \text{ Mpc}$ . Here again, as with the absolute bias, we find that star-forming galaxies above the main sequence are less clustered than star-forming galaxies below the main sequence (in run 2, “main-sequence split,” in both redshift ranges there is a  $3\sigma$ – $5\sigma$  difference on both small and larger scales). We also find that among the quiescent galaxy population, those galaxies with a higher SFR at a given stellar mass are less clustered (in run 2 at lower redshift there is a  $5\sigma$  difference on small and large scales, while at higher redshift there is an  $11\sigma$  difference on large scales). Significant differences within the star-forming and quiescent populations can also be seen in the results for run 3 (“sSFR cuts”), using finer bins in sSFR.

We also list the stellar mass and sSFR ratio between the two relevant galaxy samples in Table 5. These are defined as  $M_{*1}/M_{*2}$  and  $\text{sSFR}_1/\text{sSFR}_2$ , where 1 and 2 correspond to the galaxy samples of interest, where the relative bias is the square root of the ratio of  $w_p$  of sample 1 to  $w_p$  of sample 2. A stellar mass or sSFR ratio near unity reflects that the two galaxy samples of interest have similar stellar mass or sSFR, while ratios much larger than unity reflect that sample 1 has a much higher stellar mass or sSFR (i.e., is more highly star-forming) than sample 2. Values of these ratios that are less than unity reflect that sample 2 has a higher stellar mass or sSFR than sample 1.

The relative bias as a function of stellar mass and sSFR ratio is shown in Figure 5. The relative bias on small, “one-halo” scales is shown on the top, while the relative bias of the same

samples on larger, “two-halo” scales is shown on the bottom. We show results from runs 1, 2, 3, and 4, as well as some additional galaxy subsamples made to help create a more even distribution in stellar mass and sSFR ratios (i.e., with stellar mass ratio near unity and sSFR ratio between 0.1 and 1.0). These additional samples are very similar to those in runs 1 (star-forming/quiescent split) and 2 (main-sequence split); we simply further divide the star-forming and quiescent populations into more bins, using either a simple cut in sSFR or the tilt of the main sequence as in run 2. Instead of plotting all relative bias results, we show only those where the “one-halo” error is less than 5% of the relative bias; thus, only high signal-to-noise ratio results are shown. We show results from both redshift ranges used here and find that the relative bias between galaxy samples does not evolve strongly with redshift within the range probed here, as expected.

We find that the relative bias is a very smooth function of the sSFR ratio, declining steadily as the sSFR ratio increases, on both small and large scales. However, the relative bias is not as smooth of a function of the stellar mass ratio; at a stellar mass ratio of  $\sim 0.7$ – $2$ , there are a wide range of relative biases, in the range of  $\sim 0.7$ – $2$ . We also note that all of the high relative bias values ( $>2$  on small scales) have very low sSFR ratios ( $<0.05$ ), while they have a range of stellar mass ratios ( $1$ – $20$ ). We also find that the relative bias values are more extreme on small scales than on large scales. While the same trends are seen on both one- and two-halo scales, the trend is stronger on small scales.

In order to more clearly understand the dependence of the relative bias on stellar mass and sSFR, we show in Figure 6 the joint dependence of the two-halo relative bias on the stellar mass and sSFR ratio (the one-halo relative bias shows the same trends in this space). We highlight with dotted lines two regions of the diagram where there are multiple samples with a relatively narrow range in one ratio and a wider range in the other ratio. For example, at a stellar mass ratio near unity there are many points spanning an sSFR ratio of  $\sim 0.01$ – $10$ . As can be seen in the figure, the relative bias of these points—at a fixed stellar mass ratio—varies substantially, and monotonically, as the sSFR ratio varies. However, at a fixed sSFR ratio near  $\sim 0.03$ , for points where the stellar mass ratio varies from  $\sim 1$  to  $10$ , there is very little change in the relative bias. This clearly shows that the relative bias depends strongly on the sSFR ratio, even at a given stellar mass ratio, while the same is not true of the stellar mass ratio at given sSFR ratio. Therefore, the dependence of galaxy clustering on sSFR is stronger at a fixed stellar mass than the dependence on stellar mass at a fixed sSFR.

## 6. Discussion

In this section we compare our results to the relevant literature and discuss how our findings place constraints on how galaxies evolve in the sSFR– $M_*$  plane. We also discuss how these results impact our understanding of the mapping between galaxies and dark matter halos, including expanding the halo model of galaxy evolution to explicitly include sSFR.

### 6.1. Comparison with Literature

There are many measurements in the literature of the relative bias of quiescent to star-forming galaxies, at either a given

magnitude or stellar mass, where these two galaxy populations are defined by color, sSFR, or spectral type. Here, at a stellar mass of  $M_* \sim 10.5$ , we find a relative bias of  $2.2 (\pm 0.3)$  on one-halo scales and  $1.5 (\pm 0.1)$  on two-halo scales at  $z = 0.5$  and a relative bias of  $1.9 (\pm 0.6)$  on one-halo scales and  $1.7 (\pm 0.2)$  on two-halo scales at  $z = 0.9$ . Similar values are typically found by others, with values on large scales of  $\sim 1.3$ – $1.5$  (e.g., Madgwick et al. 2003; Meneux et al. 2006; Coil et al. 2008; de la Torre et al. 2011; Hearin et al. 2014). The relative bias of quiescent to star-forming galaxies can be a strong function of scale, however, and may be a function of stellar mass as well, so care should be taken when comparing results from different surveys.

There are also relevant results in the literature from weak-lensing studies, which directly measure halo masses around selected galaxy samples. Several studies using galaxy color have found that at a given stellar mass, red galaxies have larger halo masses than blue galaxies (Velander et al. 2014; Rodríguez-Puebla et al. 2015; Zu & Mandelbaum 2016), similar to the trends found here and in other clustering studies. Mandelbaum et al. (2016) use locally brightest galaxies in SDSS as a proxy for selecting central galaxies, in order to quantify how halo mass depends on stellar mass and color for central galaxies. They find that for  $\log(M_*/M_\odot) > 10.7$ , red central galaxies are in halos that are at least twice as massive as those of blue central galaxies, again qualitatively consistent with our findings, although we do not attempt to isolate central galaxies.

The most relevant papers to compare our results to here are those that study the dependence of clustering on multiple bins in sSFR. We present the bias reported as a function of sSFR for the relevant papers in Figure 7. Our results are somewhat higher than those of Heinis et al. (2009), but given that their sample is at  $z \sim 0.1$ , this is to be expected, as the bias decreases with cosmic time. Our results agree fairly well with those of Mostek et al. (2013), using the full DEEP2 survey at  $z \sim 0.9$ , and are much lower than Kim et al. (2015), also at  $z \sim 1$ . We also compare with results from Lin et al. (2012) at  $z \sim 2$ . The bias should decrease from  $z \sim 2$  to  $z \sim 1$  owing to the increased clustering of dark matter particles at lower redshift; the change in the growth factor over this redshift interval is  $\sim 45\%$ . Given this, it is not unexpected that our results are lower than those of Lin et al. (2012); however, we note that two of their four data points have very high bias values ( $>2.5$ ) and they do not find a monotonic trend in the bias with sSFR. The Lin et al. (2012) and Kim et al. (2015) results are derived from angular clustering measurements, which may impact their robustness. Generally, however, these results show that at a given redshift the bias decreases with increasing sSFR.

When comparing the clustering of galaxies as a function of sSFR at different redshifts, of course, the overall evolution in the normalization of the star-forming main sequence should be taken into account (e.g., Karim et al. 2011; Speagle et al. 2014; Whitaker et al. 2014). However, this evolution by itself cannot account for the sSFR dependence in clustering that is observed at a given redshift. The scatter in the main sequence does not evolve substantially with cosmic time (Speagle et al. 2014), such that essentially the sSFR of the bulk of star-forming galaxies is decreasing with time since  $z \sim 2$ . The fact that at a given epoch there is a correlation between clustering amplitude

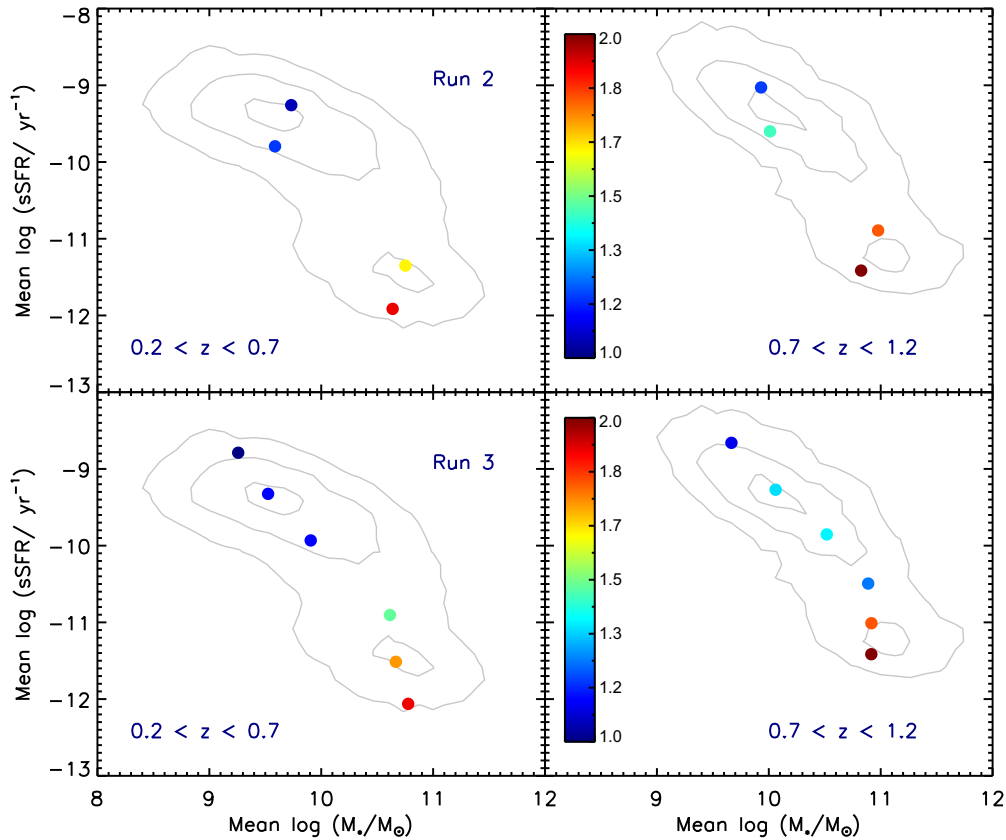


**Figure 4.** Absolute bias on scales  $1 < r_p < 10 h^{-1}$  Mpc of each galaxy sample in runs 2 (“main-sequence split”) and 3 (“sSFR cuts”), shown here as a joint function of sSFR and stellar mass. The color of each point reflects the bias value, as shown in the color bar. The light-gray contours show the full galaxy population in the relevant redshift range.

and sSFR therefore implies that galaxies evolve from having relatively high sSFR (with respect to the main sequence at that redshift) to relatively low sSFR. This is discussed more in the next section below.

We do not compare our results to stellar-mass-dependent clustering results in the literature, in part because the PRIMUS stellar-mass-dependent clustering is presented in Skibba et al. (2015) and also because here we have not necessarily included samples that are complete for all sSFRs at a given stellar mass (other than run 1, “star-forming/quiescent split”). We note, however, that not all papers that investigate the stellar-mass-dependent clustering of galaxies do use samples that are complete to all galaxy types (i.e., all sSFRs). Furthermore, because stellar mass and sSFR are not fully independent quantities for galaxies—there are correlations between them—results on the stellar mass dependence of clustering are likely impacted by differences in the sSFR of the samples. As pointed out by Coil et al. (2008) and others, the luminosity dependence of the clustering of all galaxies is stronger than the luminosity dependence present in either the star-forming or quiescent populations alone. Essentially, part of the overall luminosity dependence that is observed is due to the changing fraction of quiescent galaxies (which are more clustered) as a function of luminosity. The same holds for stellar mass and sSFR, in that the most massive galaxies have lower sSFRs, on average, at  $z \lesssim 2$ . Therefore, much of what has been interpreted as differences in galaxy clustering due to stellar mass may be driven in part by differences in sSFR.

## 6.2. Evolution of Galaxies in sSFR– $M_*$ Plane

One of the main findings of this paper is that at intermediate redshift the large-scale galaxy clustering amplitude smoothly increases across the sSFR– $M_*$  plane, from lower-mass galaxies that are forming stars at a high rate (low  $M_*$ , high sSFR; upper left corner in the lower panels of Figure 4) to higher-mass galaxies that are forming stars at a very low rate (high  $M_*$ , low sSFR; lower right corner of this figure). As the clustering of a given coeval galaxy population can generally only increase over time, this implies that galaxies evolve across the sSFR– $M_*$  plane from the upper left to the lower right. A similar conclusion is reached by Kim et al. (2015) for central galaxies, using halo occupation distribution modeling of their stellar-mass- and sSFR-dependent clustering results at  $z \sim 1$ .

This implies, interestingly, that star-forming galaxies do not simply evolve solely along the main sequence of star formation, increasing their SFR as their stellar mass increases. This is shown by the fact that at a given stellar mass, the clustering of star-forming galaxies above the main sequence is lower than that of star-forming galaxies below the main sequence (see also Mostek et al. 2013). This should perhaps not be surprising given the known differences in other galaxy physical parameters above and below the main sequence, such as SFR surface densities, sizes, dust properties, and Sérsic index (Schiminovich et al. 2007; Elbaz et al. 2011; Wuyts et al. 2011). These different physical properties are often interpreted as being due to galaxies above the main sequence experiencing merger events, but our results here do not support

**Table 5**  
Relative Bias Measurements

Run	Name	$M_*$ Ratio	sSFR Ratio	Relative Bias 1-halo <sup>a</sup>	Relative Bias 2-halo
1	red-lowz/blue-lowz	1.1	0.039	$1.98 \pm 0.08$	$1.43 \pm 0.03$
	red-highz/blue-highz	1.1	0.059	$1.56 \pm 0.14$	$1.68 \pm 0.06$
2	red1-lowz/blue2-lowz	15	0.028	$2.22 \pm 0.08$	$1.30 \pm 0.07$
	red2-lowz/blue2-lowz	11	0.0076	$2.63 \pm 0.10$	$1.60 \pm 0.04$
	blue1-lowz/blue2-lowz	1.4	3.4	$0.85 \pm 0.03$	$0.84 \pm 0.04$
	red1-lowz/red2-lowz	1.3	3.7	$0.84 \pm 0.03$	$0.81 \pm 0.04$
	red1-highz/blue2-highz	9.3	0.051	$1.99 \pm 0.19$	$1.22 \pm 0.05$
	red2-highz/blue2-highz	6.5	0.015	$2.93 \pm 0.18$	$1.79 \pm 0.06$
	blue1-highz/blue2-highz	0.83	3.7	$0.82 \pm 0.05$	$0.80 \pm 0.04$
	red1-highz/red2-highz	1.4	3.3	$0.80 \pm 0.09$	$0.68 \pm 0.03$
3	1-lowz/2-lowz	0.54	3.4	$1.06 \pm 0.11$	$0.84 \pm 0.05$
	3-lowz/2-lowz	2.4	0.25	$1.20 \pm 0.02$	$1.01 \pm 0.01$
	4-lowz/2-lowz	12	0.026	$2.15 \pm 0.08$	$1.30 \pm 0.03$
	5-lowz/2-lowz	14	0.0065	$3.01 \pm 0.10$	$1.51 \pm 0.04$
	6-lowz/2-lowz	18	0.0018	$3.13 \pm 0.13$	$1.75 \pm 0.05$
	1-highz/2-highz	0.40	4.1	$0.92 \pm 0.11$	$0.81 \pm 0.04$
	3-highz/2-highz	2.9	0.26	$1.41 \pm 0.11$	$1.02 \pm 0.03$
	4-highz/2-highz	6.7	0.060	$1.80 \pm 0.25$	$0.92 \pm 0.06$
	5-highz/2-highz	7.2	0.018	$2.18 \pm 0.23$	$1.33 \pm 0.09$
	6-highz/2-highz	7.2	0.0072	$3.97 \pm 0.32$	$2.06 \pm 0.08$
4	1-lowz/3-lowz	0.22	1.2	$0.79 \pm 0.07$	$1.05 \pm 0.08$
	2-lowz/4-lowz	0.17	1.4	$1.00 \pm 0.04$	$1.15 \pm 0.06$
	4-lowz/7-lowz	0.17	1.6	$0.86 \pm 0.06$	$1.04 \pm 0.03$
	5-lowz/8-lowz	0.22	1.1	$1.08 \pm 0.05$	$0.98 \pm 0.04$
	6-lowz/9-lowz	0.22	1.2	$1.19 \pm 0.06$	$1.13 \pm 0.05$
	1-lowz/2-lowz	0.87	3.4	$0.85 \pm 0.04$	$0.82 \pm 0.04$
	3-lowz/4-lowz	0.67	4.2	$1.17 \pm 0.11$	$0.91 \pm 0.04$
	5-lowz/6-lowz	0.89	8.7	$0.55 \pm 0.03$	$0.69 \pm 0.03$
	7-lowz/8-lowz	0.85	6.7	$0.75 \pm 0.05$	$0.77 \pm 0.03$
	8-lowz/9-lowz	0.89	9.7	$0.61 \pm 0.03$	$0.79 \pm 0.02$
	1-high/2-high	0.27	1.5	$0.59 \pm 0.08$	$0.98 \pm 0.07$
	3-high/5-high	0.22	1.8	$0.80 \pm 0.07$	$1.08 \pm 0.04$
	4-high/6-high	0.26	1.2	$0.84 \pm 0.14$	$0.56 \pm 0.09$
	3-high/4-high	0.61	12	$1.01 \pm 0.88$	$1.66 \pm 0.55$
	4-high/5-high	0.36	0.15	$0.96 \pm 0.19$	$0.69 \pm 0.13$
5-high/6-high	0.72	8.2	$0.83 \pm 0.08$	$0.82 \pm 0.05$	

**Note.**

<sup>a</sup> The “1-halo” relative bias measurements are on scales  $0.1 < r_p < 1 h^{-1}$  Mpc, and the “2-halo” measurements are on scales  $1 < r_p < 10 h^{-1}$  Mpc.

this interpretation. We do not find a rise in the clustering amplitude on small scales for star-forming galaxies above the main sequence compared to below the main sequence, and given the differences in large-scale clustering amplitude between these populations, it is clear that galaxies must begin their lives above the main sequence and evolve across it. It is therefore likely that galaxies do not solely move along the ridge of the main sequence as they grow.

We also conclude that the higher clustering amplitude seen in other studies for galaxies with higher SFR is not simply due to the fact that they have higher stellar masses (i.e., due to the star-forming main sequence). If the increase in clustering was entirely driven by differences in the stellar mass, that would imply that there should be no difference in the clustering amplitude along the main sequence of star formation. However, as shown by the results here for run 3 (“sSFR cuts”) at  $0.7 < z < 1.2$ , we find a significant increase in the bias value at the more massive end of the main sequence than at lower stellar mass on the sequence. Therefore, there must be an additional clustering dependence on SFR or sSFR beyond the

stellar mass dependence. Indeed, that is what we find when we compare the relative bias of galaxies as a function of both the stellar mass and sSFR ratio of the relevant galaxy samples.

### 6.3. Connecting Galaxies and Dark Matter Halos

We have shown that at intermediate redshift galaxy clustering correlates more strongly with sSFR than with stellar mass. A similar conclusion was also drawn by Heinis et al. (2009) with a smaller sample of sSFR bins. This conclusion is also similar to that of Coil et al. (2008), who found that at  $z \sim 1$  the dependence of clustering on color is much stronger than with luminosity, given that color is highly correlated with sSFR and luminosity correlates with stellar mass.

We find that the stellar mass of a galaxy does correlate with clustering amplitude and therefore halo mass, but much of this dependence appears to be driven by differences in sSFR. There is a correlation in the galaxy population between stellar mass and sSFR, and while higher stellar mass galaxies are more

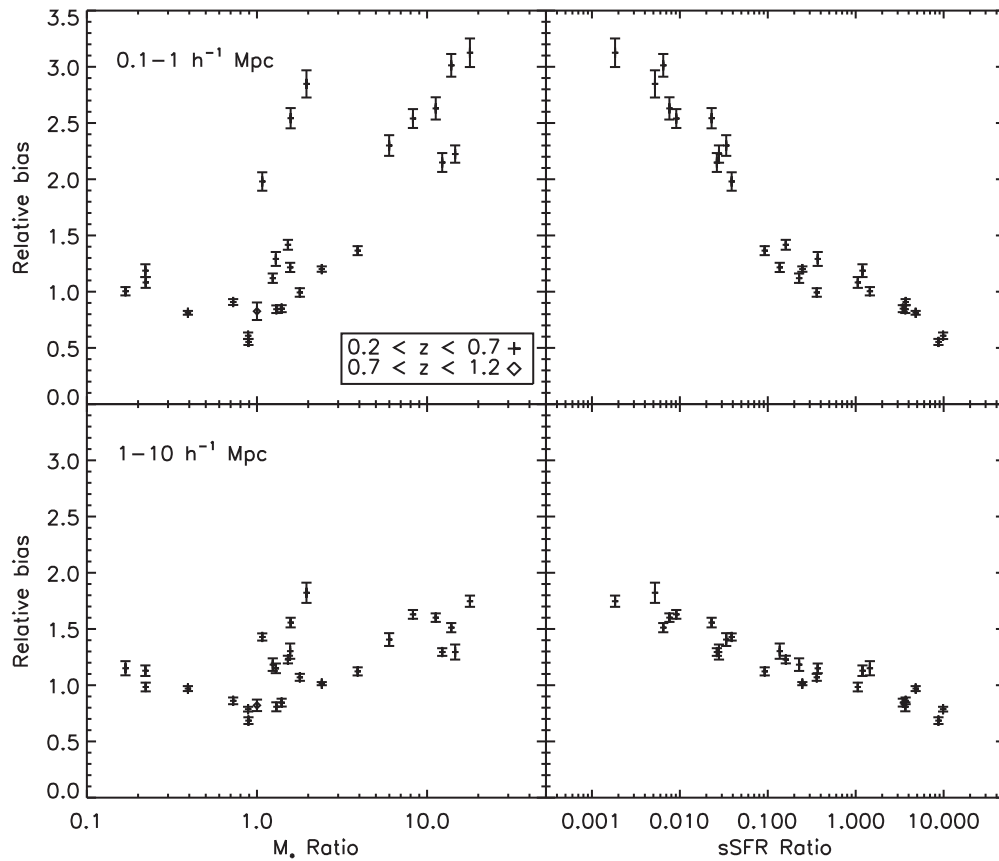


**Figure 5.** One-halo (top;  $0.1 < r_p < 1 h^{-1} \text{ Mpc}$ ) and two-halo (bottom;  $1 < r_p < 10 h^{-1} \text{ Mpc}$ ) relative bias between various galaxy samples, as a function of the stellar mass ratio (left) and sSFR ratio (right) of the two samples. Only those relative bias values with an error less than 25% of the one-halo relative bias are shown, for clarity. Additional galaxy samples are used here beyond the runs shown earlier in the paper, to help fill in this space. It can clearly be seen that the relative bias is more monotonically dependent on the sSFR ratio than the stellar mass ratio.

clustered (e.g., Skibba et al. 2014), we do not find this to be true at a given sSFR.

The halo model of galaxy evolution essentially posits that the dark matter halo mass that a galaxy resides in determines all of the galaxy’s properties (e.g., Peacock & Smith 2000; Seljak 2000). Our results would seem to counter that, in that clearly a given halo mass can correspond to a range of stellar masses for a galaxy. It is therefore not straightforward to predict the stellar mass of a galaxy, simply from knowing the halo mass that it resides in, as sSFR is another key parameter. Indeed, age-matching models (Hearin & Watson 2013) predict that at a given stellar mass, star-forming galaxies are less clustered than quiescent galaxies, as we find here. This would seem to imply that our results favor age-matching-type models over strict halo models of galaxy evolution.

However, our results cannot rule out the halo model, as at a given stellar mass, satellite galaxies are found to reside in somewhat more massive halos than central galaxies (Watson & Conroy 2013) and satellite galaxies of a given stellar mass (in more massive halos) are more likely to be quiescent than central galaxies in lower-mass halos (Wetzel et al. 2012). This can lead to a higher clustering amplitude for quiescent galaxies compared to star-forming galaxies at a given stellar mass, without invoking assembly bias, which posits that another property of the halo besides mass is relevant in determining galaxy properties. In other words, both star-forming and

quiescent central galaxies of the same stellar mass could have the same clustering amplitude, while comparing the clustering of all galaxies (including satellites) of that stellar mass, quiescent galaxies would be more clustered, as they include more satellites in higher-mass halos. Our results therefore do not necessarily imply assembly bias; a detailed comparison with halo models and models that include assembly bias is required to make that claim. However, Berti et al. (2016) measure the galaxy conformity signal in PRIMUS, essentially through a cross-correlation of isolated, massive galaxies with lower-mass, star-forming galaxies, and find a signal that likely does reflect assembly bias at these redshifts.

We note that much of the stellar mass dependence that previous papers have found in galaxy clustering may be influenced by differences in the sSFR of the galaxy samples used, given the correlation between stellar mass and sSFR within the full galaxy population (and within the star-forming and quiescent populations separately). We find that at a given stellar mass, star-forming galaxies are significantly less clustered than quiescent galaxies, which implies that halo mass must depend jointly on stellar mass and sSFR. The relation of stellar mass to halo mass, then, likely needs to be expanded to account for sSFR. This would essentially involve shifting the relation of stellar mass to halo mass to higher or lower halo masses depending on the sSFR of the galaxy in question. The scatter that has been quantified in the relation of stellar mass to

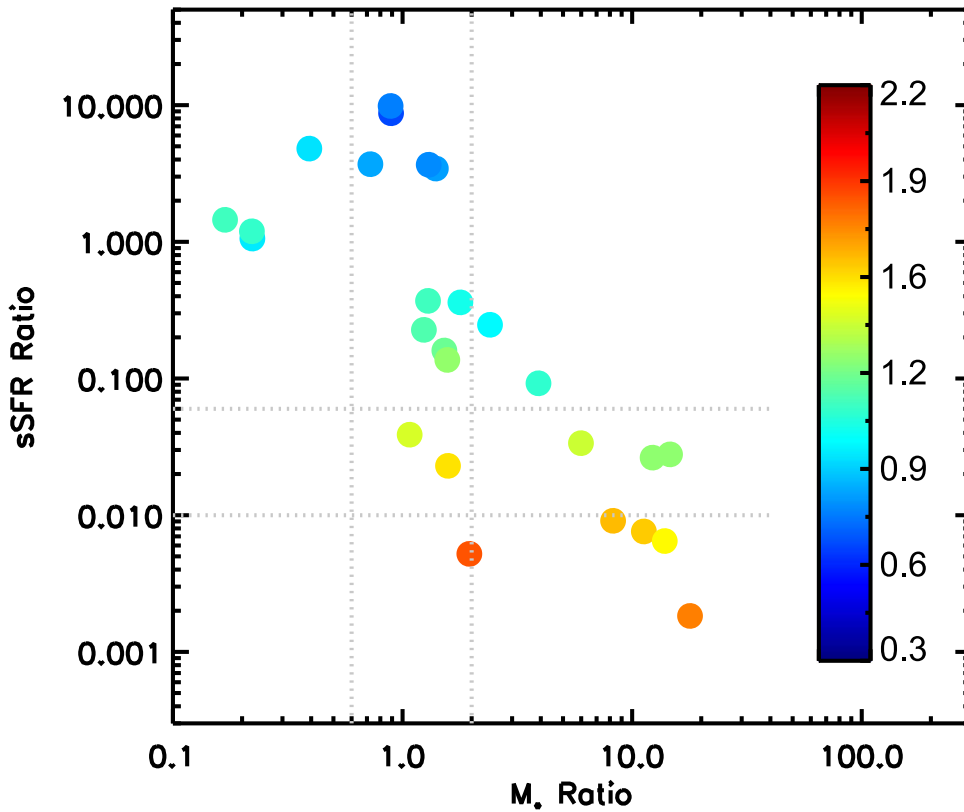


**Figure 6.** Two-halo relative bias between various galaxy samples, shown as a joint function of sSFR ratio and stellar mass ratio. Shown are all relative biases where the fractional error is less than 25%. The color of each point reflects the relative bias value, as shown in the color bar. The dotted lines highlight regions of fixed stellar mass or sSFR ratio where our galaxy samples are able to probe at least an order of magnitude in the ratio of the other parameter (stellar mass or sSFR). As seen, at a fixed stellar mass ratio, variations with sSFR lead to strong differences in the relative bias, while at a fixed sSFR ratio, variations with stellar mass do not result in substantially different clustering amplitudes.

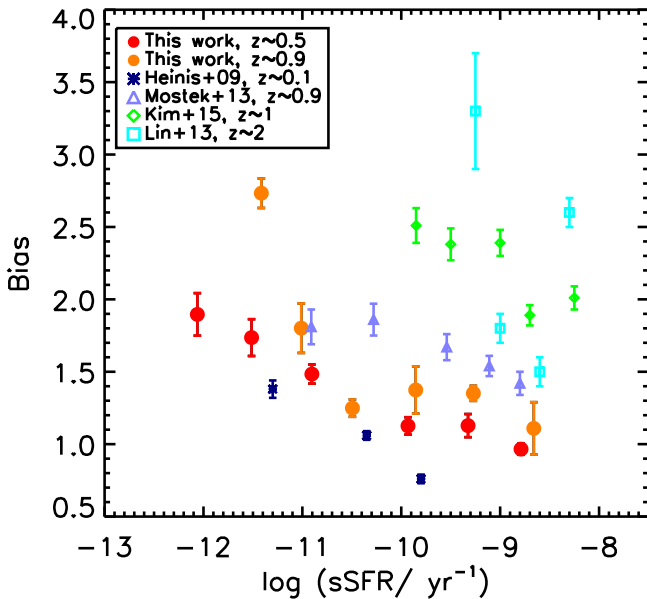


**Figure 7.** Two-halo absolute bias of galaxies as a function of sSFR for our results in comparison to other results in the literature at  $z \sim 1-2$  (Lin et al. 2012; Mostek et al. 2013; Kim et al. 2015).

halo mass (e.g., More et al. 2011; Moster et al. 2013; Behroozi et al. 2013) may be due in part to sSFR. The sSFR of a galaxy appears to be in fact more correlated with halo mass than stellar

mass correlates with halo mass. While it is likely that much of this reflects that the red fraction of satellite galaxies increases with halo mass (even at a given stellar mass; e.g., Prescott et al. 2011), it also seems likely that even for central galaxies there is a dependence on sSFR at a given halo mass. Indeed, below the break in the stellar mass function, halo mass does not strongly correlate with stellar mass, though our results suggest that it may correlate with sSFR.

Finally, we note that the relative bias results presented here as a function of the joint dependence on the stellar mass ratio and sSFR ratio provide very strong constraints for theoretical models of galaxy evolution. They are also a new way of using the data to measure the dependence of galaxy clustering on these parameters. This new measurement of the joint dependence of the relative bias on ratios of galaxy properties should help differentiate between competing theoretical models of galaxy evolution.

## 7. Conclusions

In this paper we have used the PRIMUS and DEEP2 galaxy redshift surveys to study the joint dependence of galaxy clustering properties on stellar mass and sSFR. We utilize a full sample of over 100,000 spectroscopic redshifts to divide our sample into two redshift ranges,  $0.2 < z < 0.7$  and  $0.7 < z < 1.2$ , and use SED fits to estimate the galaxy stellar mass and sSFR. Not only do we divide the full galaxy population into star-forming and quiescent samples, but we

also subdivide each of these populations according to sSFR or distance from the main sequence of star formation, to study the dependence of the clustering amplitude in relatively fine bins in sSFR. We measure both the absolute bias of galaxy samples with respect to dark matter and the relative bias between galaxy samples, as a joint function of the ratio of the stellar masses and sSFRs of the galaxy samples.

Our main conclusions are as follows.

1. Galaxy clustering depends just as strongly on sSFR as on stellar mass, within the stellar mass range probed here. Our results imply that the relation of stellar mass to halo mass may depend on sSFR as well.
2. Within the star-forming population at a given stellar mass, galaxies with a high sSFR that lie above the main sequence are less clustered than galaxies with a relatively low sSFR below the main sequence. This is also true within the quiescent population, in that galaxies with a higher sSFR are less clustered than galaxies with a lower sSFR, at a given stellar mass. This constrains the evolutionary path of galaxies in the sSFR–stellar mass plane, indicating that they likely evolve from high sSFR and lower stellar mass to low sSFR and higher stellar mass. In particular, galaxies likely evolve across the main sequence of star formation, not only along it, before becoming quiescent. Within the quiescent population, galaxies with higher sSFR are likely also younger, on average, than those with lower sSFR.
3. We present new measurements of the relative bias of galaxies as a joint function of the stellar mass ratio and sSFR ratio of galaxy samples, showing that at a given stellar mass ratio there is a strong dependence of clustering amplitude on the sSFR ratio. The reverse is not true, however; at a given sSFR ratio there does not appear to be a strong dependence of the clustering amplitude on the stellar mass ratio. This shows that while galaxy clustering depends on stellar mass, it does not depend on stellar mass at a given sSFR, within the range of stellar mass and sSFR probed here.

These results are strongly constraining for theoretical models of galaxy evolution, both for age-matching and other empirically based methods (e.g., Behroozi et al. 2013), as well as semianalytic models. It would clearly be beneficial to perform similar investigations at both lower and higher redshift. Such measurements, undertaken across a range of redshifts and cosmic time, would be extremely constraining for theoretical models of galaxy evolution and the galaxy–halo connection.

We thank Andrew Hearin and Peter Behroozi for useful discussions and the referee for detailed comments. Funding for PRIMUS has been provided by NSF grants AST-0607701, 0908246, 0908442, and 0908354 and NASA grant 08-ADP08-0019. A.L.C. acknowledges support from NSF CAREER award AST-1055081. We use data from the DEEP2 survey, which was supported by NSF AST grants AST00-71048, AST00-71198, AST05-07428, AST05-07483, AST08-07630, and AST08-08133. This study makes use of data from the AEGIS Survey and in particular uses data from *GALEX*, *Spitzer*, CFHT, and the Keck and Magellan telescopes.

## References

- Alimi, J.-M., Valls-Gabaud, D., & Blanchard, A. 1988, *A&A*, **206**, L11
- Baldry, I. K., Glazebrook, K., Brinkmann, J., et al. 2004, *ApJ*, **600**, 681
- Behroozi, P. S., Conroy, C., & Wechsler, R. H. 2010, *ApJ*, **717**, 379
- Behroozi, P. S., Wechsler, R. H., & Conroy, C. 2013, *ApJ*, **770**, 57
- Benoist, C., Maurogordato, S., da Costa, L. N., Cappi, A., & Schaeffer, R. 1996, *ApJ*, **472**, 452
- Berlind, A. A., Blanton, M. R., Hogg, D. W., et al. 2005, *ApJ*, **629**, 625
- Berti, A., Coil, A. L., Behroozi, P. S., et al. 2016, *ApJ*, **801**, 88
- Bigelow, B. C., & Dressler, A. M. 2003, *Proc. SPIE*, **4841**, 1727
- Blanton, M. R., & Roweis, S. 2007, *AJ*, **133**, 734
- Bruzual, G., & Charlot, S. 2003, *MNRAS*, **344**, 1000
- Chabrier, G. 2003, *PASP*, **115**, 763
- Charlot, S., & Fall, S. M. 2000, *ApJ*, **539**, 718
- Coil, A. L., Blanton, M. R., Burles, S. M., et al. 2011, *ApJ*, **741**, 8
- Coil, A. L., Davis, M., Madgwick, D. S., et al. 2004b, *ApJ*, **609**, 525
- Coil, A. L., Newman, J. A., Cooper, M. C., et al. 2006, *ApJ*, **644**, 671
- Coil, A. L., Newman, J. A., Croton, D., et al. 2008, *ApJ*, **672**, 153
- Coil, A. L., Newman, J. A., Kaiser, N., et al. 2004a, *ApJ*, **617**, 765
- Coil, R. J., Moustakas, J., Blanton, M. R., et al. 2013, *ApJ*, **767**, 118
- Davis, M., & Peebles, P. J. E. 1983, *ApJ*, **267**, 465
- de la Torre, S., Le Fèvre, O., Porciani, C., et al. 2011, *MNRAS*, **412**, 825
- Dolley, T., Brown, M. J. I., Weiner, B. J., et al. 2014, *ApJ*, **797**, 125
- Durkalec, A., Le Fèvre, O., de la Torre, S., et al. 2015, *A&A*, **576**, L7
- Elbaz, D., Dickinson, M., Hwang, H. S., et al. 2011, *A&A*, **533**, A119
- Faber, S. M., Phillips, A. C., Kibrick, R. I., et al. 2003, *Proc. SPIE*, **4841**, 1657
- Hearin, A. P., & Watson, D. F. 2013, *MNRAS*, **435**, 1313
- Hearin, A. P., Watson, D. F., Becker, M. R., et al. 2014, *MNRAS*, **444**, 729
- Heinis, S., Budavári, T., Szalay, A. S., et al. 2009, *ApJ*, **698**, 1838
- Hogg, D. W., Blanton, M. R., Eisenstein, D. J., et al. 2003, *ApJL*, **585**, L5
- Karim, A., Schinnerer, E., Martínez-Sansigre, A., et al. 2011, *ApJ*, **730**, 61
- Kim, J.-W., Im, M., Lee, S.-K., et al. 2015, *ApJ*, **806**, 189
- Landy, S. D., & Szalay, A. S. 1993, *ApJ*, **412**, 64
- Leauthaud, A., Tinker, J., Behroozi, P. S., Busha, M. T., & Wechsler, R. H. 2011, *ApJ*, **738**, 45
- Leauthaud, A., Tinker, J., Bundy, K., et al. 2012, *ApJ*, **744**, 159
- Li, C., Kauffmann, G., Heckman, T. M., Jing, Y. P., & White, S. D. M. 2008, *MNRAS*, **385**, 1903
- Li, C., Kauffmann, G., Jing, Y. P., et al. 2006, *MNRAS*, **368**, 21
- Lin, L., Dickinson, M., Jian, H.-Y., et al. 2012, *ApJ*, **756**, 71
- Lonsdale, C. J., Smith, H. E., Rowan-Robinson, M., et al. 2003, *PASP*, **115**, 897
- Loveday, J., Maddox, S. J., Efstathiou, G., & Peterson, B. A. 1995, *ApJ*, **442**, 457
- Madau, P., & Dickinson, M. 2014, *ARA&A*, **52**, 415
- Madgwick, D. S., Hawkins, E., Lahav, O., et al. 2003, *MNRAS*, **344**, 847
- Mandelbaum, R., Wang, W., Zu, Y., et al. 2016, *MNRAS*, **457**, 3200
- Marulli, F., Bolzonella, M., Branchini, E., et al. 2013, *A&A*, **557**, A17
- Mathews, D. J., Newman, J. A., Coil, A. L., Cooper, M. C., & Gwyn, S. D. J. 2013, *ApJS*, **204**, 21
- Meneux, B., Guzzo, L., de la Torre, S., et al. 2009, *A&A*, **505**, 463
- Meneux, B., Guzzo, L., Garilli, B., et al. 2008, *A&A*, **478**, 299
- Meneux, B., Le Fèvre, O., Guzzo, L., et al. 2006, *A&A*, **452**, 387
- More, S., van den Bosch, F. C., Cacciato, M., et al. 2011, *MNRAS*, **410**, 210
- Moster, B. P., Naab, T., & White, S. D. M. 2013, *MNRAS*, **428**, 3121
- Moster, B. P., Somerville, R. S., Maulbetsch, C., et al. 2010, *ApJ*, **710**, 903
- Mostek, N., Coil, A. L., Cooper, M., et al. 2013, *ApJ*, **767**, 89
- Moustakas, J., Coil, A. L., Aird, J., et al. 2013, *ApJ*, **767**, 50
- Newman, J. A., Cooper, M. C., Davis, M., et al. 2013, *ApJS*, **208**, 5
- Noeske, K. G., Weiner, B. J., Faber, S. M., et al. 2007, *ApJL*, **660**, L47
- Norberg, P., Baugh, C. M., Hawkins, E., et al. 2001, *MNRAS*, **328**, 64
- Norberg, P., Baugh, C. M., Hawkins, E., et al. 2002, *MNRAS*, **332**, 827
- Oliver, S., Rowan-Robinson, M., Alexander, D. M., et al. 2000, *MNRAS*, **316**, 749
- Peacock, J. A., & Smith, R. E. 2000, *MNRAS*, **318**, 1144
- Peebles, P. J. E. 1980, *The Large-scale Structure of the Universe* (Princeton: NJ Princeton Univ. Press)
- Pierre, M., Valtchanov, I., Altieri, B., et al. 2004, *JCAP*, **9**, 11
- Pollo, A., Guzzo, L., Le Fèvre, O., et al. 2006, *A&A*, **451**, 409
- Prescott, M., Baldry, I. K., James, P. A., et al. 2011, *MNRAS*, **417**, 1374
- Rodríguez-Puebla, A., Avila-Reese, V., Yang, X., et al. 2015, *ApJ*, **799**, 130
- Schimminovich, D., Wyder, T. K., Martin, D. C., et al. 2007, *ApJS*, **173**, 315
- Scoville, N., Aussel, H., Brusa, M., et al. 2007, *ApJS*, **172**, 1
- Seljak, U. 2000, *MNRAS*, **318**, 203

- Skibba, R. A., Coil, A. L., Mendez, A. J., et al. 2015, *ApJ*, 807, 152
- Skibba, R. A., Smith, M. S. M., Coil, A. L., et al. 2014, *ApJ*, 784, 128
- Smith, R. E., Peacock, J. A., Jenkins, A., et al. 2003, *MNRAS*, 341, 1311
- Sobral, D., Best, P. N., Geach, J. E., et al. 2010, *MNRAS*, 404, 1551
- Speagle, J. S., Steinhardt, C. L., Capak, P. L., & Silverman, J. D. 2014, *ApJS*, 214, 15
- Strateva, I., Ivezić, Ž., Knapp, G. R., et al. 2001, *AJ*, 122, 1861
- Velander, M., van Uitert, E., Hoekstra, H., et al. 2014, *MNRAS*, 437, 2111
- Wake, D. A., Whitaker, K. E., Labbé, I., et al. 2011, *ApJ*, 728, 46
- Watson, D. F., & Conroy, C. 2013, *ApJ*, 772, 139
- Watson, D. F., Hearin, A. P., Berlind, A. A., et al. 2015, *MNRAS*, 446, 651
- Wetzel, A. R., Tinker, J. L., & Conroy, C. 2012, *MNRAS*, 424, 232
- Whitaker, K. E., Franx, M., Leja, J., et al. 2014, *ApJ*, 795, 104
- Wuyts, S., Förster Schreiber, N. M., van der Wel, A., et al. 2011, *ApJ*, 742, 96
- Zehavi, I., Zheng, Z., Weinberg, D. H., et al. 2005, *ApJ*, 630, 1
- Zehavi, I., Zheng, Z., Weinberg, D. H., et al. 2011, *ApJ*, 736, 59
- Zu, Y., & Mandelbaum, R. 2016, *MNRAS*, 457, 4360